2013

Development of hybrid inorganic-organic light-emitting devices with metal oxide charge transport layers

Rajeev Acharya
West Virginia University

Development of hybrid inorganic-organic light-emitting devices with metal oxide charge transport layers

Rajeev Acharya

Thesis submitted to

The Benjamin M. Statler College of Engineering and Mineral Resources

at West Virginia University

in partial fulfillment of the requirements

for the degree of

Master of Science
in
Electrical Engineering

Xian-An Cao, Ph.D., Chair

Yuxin Liu, Ph.D.

Charter D. Stinespring, Ph.D.

Lane Department of Computer Science and Electrical Engineering

Morgantown, West Virginia 2013

Keywords: Metal oxide; Light-emitting diode, Hybrid inorganic-organic light-emitting diode

Abstract

Development of hybrid inorganic-organic light-emitting devices with metal oxide charge transport layers

Rajeev Acharya

Organic light emitting diodes (OLEDs) are currently being considered as the next generation technology in flat panel displays and solid state lighting applications. Among which, phosphorescent organic light emitting diodes (PhOLEDs) with nearly 100% internal quantum efficiency including other properties such as self emitting, high luminescence efficiency, broad wavelength range, wide viewing angle, high contrast, low power consumption, low weight, and large emitting area are gaining popularity in both academic and industrial research. Although development and commercialization of OLED technology is growing, there are still several key issues that need to be addressed – the external quantum efficiency (EQE) needs to be improved and the biggest technical challenge is to increase the device operational lifetime. Balanced charge injection and transport is vital for improving the device efficiency which demands for selection of better charge injection and transport materials. In addition imbalanced charge injection also degrades the device via joule's heating and charge accumulation thereby limiting the device lifetime. Sensitivity of organic materials to the ambient atmosphere, particularly oxygen and moisture impedes the device performance.

This thesis work attempts to address these issues in the PhOLEDs through selection of proper charge injection and transport material as well as device structure optimization. At first we prepared thin films of thermally evaporated zinc-tin oxide (ZTO) with various ZnO and SnO_2

compositions and studied its optical, electrical and morphological properties. After optimization of transparency and conductivity, these ZTO films showed promising materials for alternate transparent conducting oxides and electron transport layer (ETL) functions. Similarly, thin films of thermally evaporated tungsten oxide (WO_3) were prepared and their optical and electrical properties were studied and evaluated as a hole transport layer (HTL) material. We then fabricated and characterized various hybrid light emitting diode (HyLED) structures comprising of – ZTO as an ETL, WO_3 as a HTL, and MoO_3 as a hole injecting layer (HIL). The device structures were optimized for better performance in terms of efficiency and operational lifetime. Significant enhancement in EQE and operational lifetime were obtained in HyLEDs having WO_3 as a HTL than of PhOLEDs with organic HTL. This is because WO_3 improved hole injection as well as enabled facile hole transport thereby maintaining the balance of charge injection into the device. Finally, we also prepared inverted HyLEDs using WO_3 as HTL and several metals including Ca, Ca/LiF, and Al/LiF as a cathode and their electron injecting capability were studied. Balanced charge injection was observed when a nanometer thick Ca was used as a cathode and WO_3 as a HTL. As a result, inverted HyLED with better EQE and operational lifetime were fabricated.

ACKNOWLEDGEMENTS

First, I would like to thank my advisor, Prof. Xian-An Cao for his guidance, patience, support during the past two years and allowing me to work in an interesting research topic of hybrid inorganic-organic light emitting diodes. I would also like to thank Prof. Charter D. Stinespring and Prof. Yuxin Liu for their availability as a committee member and their helpful input and invaluable time.

I wish to thank, Dr. Kolin Brown of WVU Shared Research Facility (SRF) for all the technical and non-technical discussions and suggestions. I further wish to thank Dr. Weiqiang Ding, Harley Hart for training me with the SRF instruments as well as teaching the basic maintenance and handling of them.

My special gratitude goes to my lab mates, Dr. Yiqiang Zhang, who introduced me to the handling and working of the equipments, and most recently Yifei Liu, Xiaomong Li for the discussions, lab assistance and support. I will also take this chance to thank fellow lab mates for providing a pleasant work environment in the shared facilities.

Finally, I would like to thank my parents, whose constant belief, love and support has given me all the strength and self-motivation; and to whom I dedicate this thesis.

TABLE OF CONTENTS

List of Figures

Chapter 1

Introduction

1.1 A brief History of organic light-emitting diodes (OLEDs)

Electroluminescence (EL) is a phenomenon of light generation in a certain class of materials from the application of an external electric field by the process of radiative decay of the excited state of atoms or molecules within the materials [1]. EL consists of a sequence of physical processes including, charge injection (injection of electrons and holes from electrodes), charge transport, exciton formation, and photon emission (radiative recombination of excitons).

The first discovery of EL from in-organic materials (ZnS) was made by Destriau *et al* in 1936 [1], while from an organic molecule, anthracene, was reported by Pope and coworkers in 1963 [2]**.** The reported EL from anthracene was observed when a bias of several hundred volts was applied across a 10 μm-thick layer. In 1965 W. Helfrich and W.G. Schneider demonstrated double injection EL for the first time in an anthracene single crystal by injecting electrons and holes from separate electrodes [3]. In 1982, Vincent et al. used vacuum deposited organic thin films (0.6 μm) to achieve EL. Though the operation voltage was lowered below 100 V, the external quantum efficiency (EQE) remained very low, below (0.05%) [4]. In 1970s, EL from polymer films were first observed by R. Patridge at the National Physical Laboratory in the UK, and the first polymer light emitting diode (PLED) consisting of a film of poly(*N*-vinylcarbazole) (PVK) was reported. The results were patented in 1975 and published in 1983 [5-8]. However, due to very low conductivity of the polymer films, a very high driving voltage was required which limited the output power and efficiency of the device.

The first report of efficient and low-voltage OLEDs by Tang and VanSlyke in 1987 [9] drew serious attention in the OLED technology. The OLED was based on a simple p-n heterostructure consisting of a layer N, N'- diphenyl -N, N'-bis (3-methylphenyl) 1,1'-biphenyl-4, 4' diamine (TPD) as the hole transport layer and tris(8-hydroxyquinoline) aluminum (Alq3) as both the electron transport layer and the light emission layer. While working at Eastman Kodak, they developed OLEDs with the luminance of over 1000 Cd/m^2 at ~ 10 V. In 1990 J. H. Burroughes *et al.* from Cavendish Lab. in Cambridge reported green PLEDs with a low driving voltage based on poly(*p*-phenylene vinylene) (PPV) [10].

Fluorescence due to the singlet exciton recombination is the main mechanism of light emission from the OLEDs developed by Tang et al. Spin statistics results confirmed that three out of four generated excitons are triplets, therefore limiting the ideal maximum fluorescent yield to be 25%. In 1998, M.A. Baldo et al [11] demonstrated OLED using doped phosphorescent organic molecule 2,3,7,8,12,13,17,18-octaethyl-21H,23H-porphine platinum(II) (PtOEP) as the lumiphores, called phosphorescent OLED (PhOLED), where the EL was due to triplet exciton recombination. The device can therefore overcome the 25% limit on the internal quantum efficiency of fluorescent OLEDs. In late 1990s and early 2000s, several groups made significant efforts to develop high-efficiency PhOLEDs based on Ir (III) complexes, and pushed the IQE of PhOLEDs close to unity. These progresses in the development of efficient OLEDs have attracted extensive research and studies, and rendered it a potential next generation technology for displays and lighting applications.

1.2 Organic semiconductor materials: small molecules and polymers

Carbon based organic materials have been used in electronics industry pertaining to its insulating property until the discovery of conducting polymers in 1976. The emergence of a new class of conducting organic materials, called π-conjugated organic materials, opened doors to their use in various optoelectronic devices. The first class of conducting polymers was developed in 1977, when high conductivity was observed in polyacetylene [12]. This marked the beginning of a new era of developing organic electronics.

Carbon has a ground state electronic configuration of $1s^2$, $2s^2$ and $2p^2$. This configuration allows carbon to form two possible hybridizations – sp^2 and sp^3 (figure 1.1).

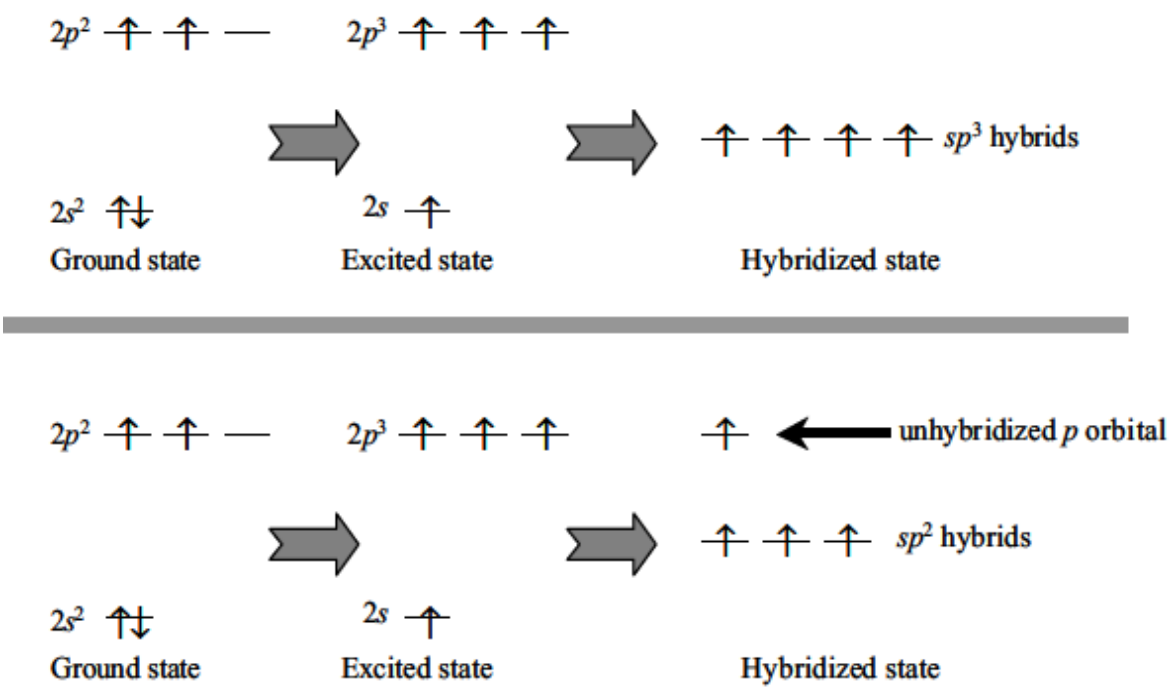

Figure 1.1 Hybridization of the valence shell electrons of a carbon atom. The upper and lower panel show sp^3 and sp^2 hybridization respectively [13]

Sp^3 hybridization allows carbon to form a tetrahedral structure having valency of four thereby forming four covalent bonds. With this type of structure, the organic materials appear to be insulating. (For example, polyethelene). In contrast, with sp^2 hybridization, carbon forms hexagonal covalent bonds, giving rise to the conjugated or semiconducting organic molecules, such as polyacetylene. Three sp^2 hybridized orbital forms sigma (σ) bonds, whereas one unhybridized pz-orbital that lies perpendicular to the sp^2 plane forms the pi-bond (π-bond). Sigma bonds set up the back bone of the material whereas π-bonds enable electrical conductivity.

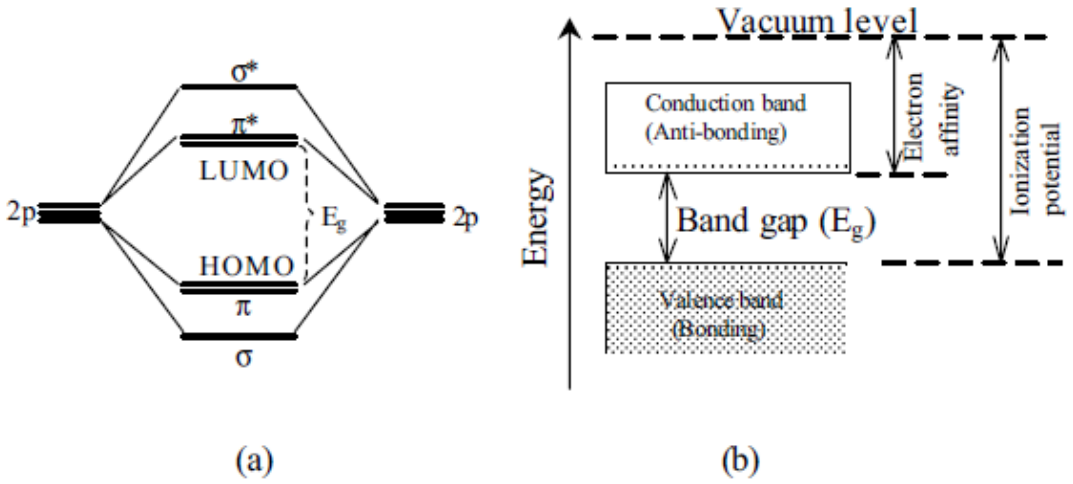

Figure 1.2 Energy level splitting of orbitals in a conjugated polymer according to molecular orbital theory (a) HOMO and LUMO level referring to the π- and π*-bands (b) Collection of molecular orbitals forming bands separated by an energy gap [14].

A Linear combination of the directed covalent bonds (σ-bonds) from each repeating unit forms a low energy bonding sigma band (σ-band) and a high energy anti-bonding sigma band (σ*-band) (figure 1.2 a), holding the molecule together. The splitting of σ and σ* bands is about 10 eV. Similarly, A linear combination of un-hybridized p_z orbitals forms low energy bonding

pi-band (π-band) and a high energy anti-bonding pi-band (π*-band). The energy levels of the Bonding and anti-bonding pi-bands lie in between those of the σ- band and σ*- band (figure 1.2 b).

The higher energy anti-bonding π*-orbitals form the conduction band whereas the lower energy bonding π-orbitals form the valence band of the material. The two bands are separated by a material specific energy gap known as a band gap (Eg). The two separated bands are characterized by two quite important energy levels, namely, the electron affinity and ionization potential. The Electron affinity corresponds to the lowest state of the conduction band (π* state), known as the lowest unoccupied molecular orbital (LUMO) in organic materials. Likewise, the ionization potential refers to the upper state of the valence band (π state), known as the highest occupied molecular orbital (HOMO) in organic materials. The band gaps of typical π-conjugated molecules and polymers determined from optical and other spectroscopic measurements are within the semiconducting range of 1 to 4 eV.

Unlike in inorganic semiconductors, electron and hole in organic semiconductors are bound together by the Coulomb force. This bounded pair of electron and hole carrying no net charge is called an exciton. The Low dielectric constant of organic materials gives rise to a strong binding energy to the exciton. Due to a small the wave function overlap of electrons and holes, the recombination of the exciton is slow. This leads to a long lifetime of the exciton, on the order of nanoseconds. When excitons in these materials recombine radiatively within their lifetime, luminescence occurs.

Excitons can be classified on the basis of their radii and spins -

(i) On the basis of exciton radii

Frenkel type excitons – When the dielectric constant of a material is very small (~2-10) , the Coulomb force of attraction between an electron and an hole is very strong, which tends to reduce the distance between the electon and hole. Therefore, the resulting exciton radius approaches the size of the unit cell or that of molecule in case of polymers. This type of excitons which sit on the same molecule are know an Frenkel type excitons.

Mott-Wannier type excitons – When a material's dielectric constant is large (>20), then the exciton binding energy is small. The exciton radius is larger than the lattice spacing or the size of the molecule. These excitons, called Mott-Wannier excitons, are typically found in polymers and oriented along the direction of the polymer chain .

(ii) On the basis of exciton spin

Singlet excitons – When an exciton is formed without the spin inversion of a transition electron, then the net spin of the exciton is zero. Such type of excitons are known as singlet excitons.

Triplet excitons – When there is spin inversion during the transition of an electron, then the net spin of the formed exciton is one. Such excitons are known as triplet excitons.

A Simplified, Jablonski diagram in figure 1.3 shows various competing processes involved during exciton generation and recombination. Electrons from higher singlet states (S2, S3..) relax down to the lowest singlet excited state S1 in a time scale of femtoseconds through a Internal Conversion (IC) process. This transition occurs without spin inversion of an electron. Once the electrons are in the S1 states, one of two processes, either Fluorescence or Intersystem Crossing (ISC), can occur. The radiative decay between the lowest excited singlet state S1 and

the ground state S0 causes fluorescence. Fluorescence of singlet excitons is observed in the time scales of ~ 10^{-9} to 10^{-8} sec. ISC is the transition of excitons from S1 to T1 states with the reversal of electron spin at a rate of picoseconds. As a result, triplet excitons are formed. Radiative decay between the lowest triplet state T1 and the ground state S0 causes phosphorescence, whose time scale is much longer, on the order of ~ 10^{-6} to 10 sec.

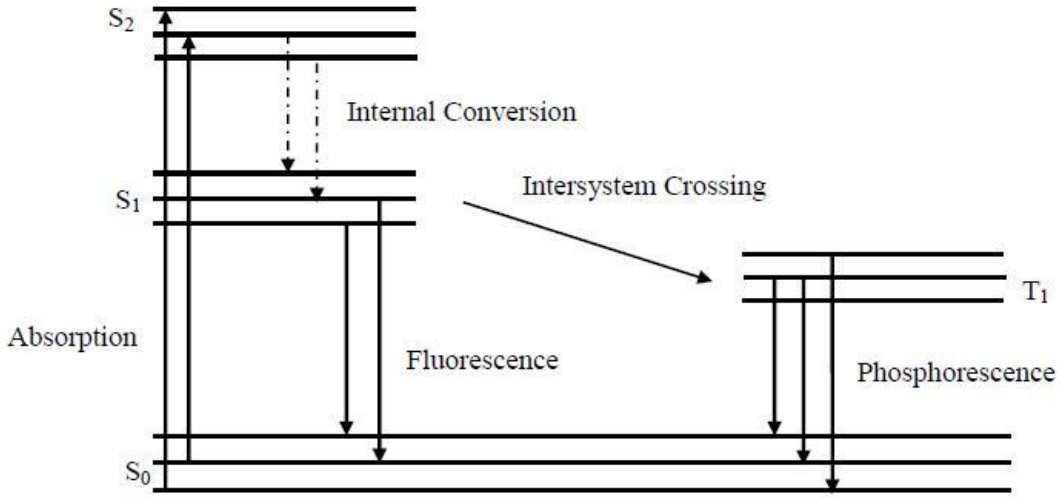

Figure 1.3 Jablonski diagram showing absorption, fluorescence, phosphorescence and intersystem crossing

Since, spin inversion of an electron is involved during the formation of triplet excited states; this is less probable in normal molecular excitation. Triplet T_1 to ground state S_0 singlet transitions giving phosphorescence is therefore forbidden. However, it is more favorable when the spin-orbital coupling is considered in some special molecular complexes. In quantum mechanics, spin-orbital coupling is the phenomenon of interaction between the spin and the motion of a particle. The spin orbital interaction is proportional to Z^8, where Z is that atomic number of the atom [14]; therefore, phosphorescence is favorable in the organo-metallic complexes containing heavy metal atoms such as Iridium, Platinum etc. In addition, spin-orbit

coupling is also responsible for transition between the lowest excited singlet states S_1 to the lowest excited triplet state T_1, called ISC. Since, energy of T_1 is lower than the S_1 state, therefore it is more favorable for an S_1 excited state to relax via ISC to the T_1 triplet state and followed by phosphorescence emission than the fluorescence.

1.3 Typical Structure of phosphorescent OLEDs (PhOLEDs)

The first small molecule OLEDs had a simple structure, consisting of two organic layers, the TPD hole transport layer and Alq3 emitting and electron transport layers, between the anode and cathode [15]. During decades of OLEDs technology development, the structure has become more complicated, containing multilayer of nanometer-thick organic layers, especially for PhOLEDs based on small molecule organic materials.

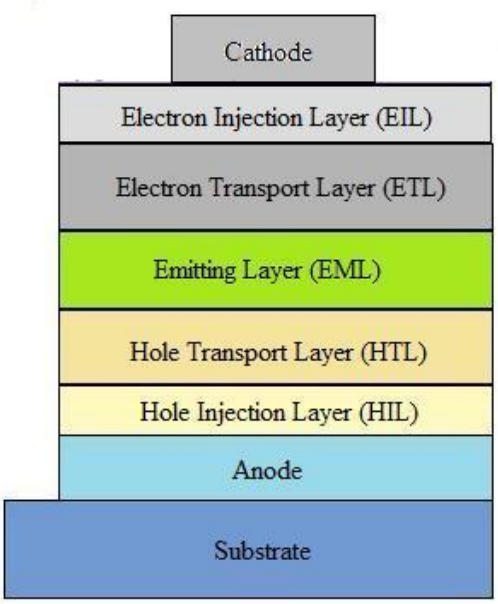

Figure 1.4 A simple PhOLED structure

Typical PhOLEDs may contain several different organic layers sandwiched between the cathode and anode The layers include the hole injection layer (HIL), hole transport layer (HTL), emitting layer (EML), electron transport layer (ETL), and electron injection layer (EIL), as shown in Fig. 1.4. The HIL (EIL) acts as a buffer layer between the anode (cathode) and the adjacent HTL (ETL) reduces the hole (electron) injection barrier and thus facilitates charge injection. The HTL (ETL) transports the injected holes (electrons) to the recombination zone located within the EML. A good HTL (ETL) acts as an electron (hole) blocking layer as well. The EML typically comprises a host material doped with a phosphorescent guest material.

Phosphorescent molecules used in PhOLEDs are typically organo-metallic complexes, consisting of a heavy metal atom, such as iridium [16], platinum [17], at the center of the molecule. Ir $(ppy)_3$ is an example of green light-emitting phosphorescent organic molecules. This large center atom facilitates formation of more triplet excitons via inter system crossing (ISC), allowing strong spin-orbit interactions. As a consequence, the lifetime of triplet excitons is increased and the phosphorescence phenomenon is observed within these molecules and a large density of triplet excitons are generated, resulting in strong phosphorescence [18, 19]. Therefore, light output from PhOLEDs is contributed by both singlet and triplet exciton recombination, allowing the internal quantum efficiency to reach nearly 100% [16].

By properly selecting the material in the EML, the color of OLEDs can be varied from UV to red, covering the whole visible range. Common Fluorescent materials used in OLEDs include 4,4'-bis(carbazol-9-yl)biphenyl (CBP), which emits in the near UV to deep violet, 4,4 '-bis(2,2 ' diphenyl vinyl)-1,1 '-biphenyl (DPVBi) emitting in blue, Alq3 emitting in the green, and 4-(dicyano-methylene)-2-methyl-6-julolidyl-9-enyl-4H-pyran (DCM2) emitting in red [20-22]. Among phosphorescent materials, FIrpic emits in the skyblue, Ir$(ppy)_3$ in the green, and PtOEP

in the red [11,16,17]. Some materials are multifunctional. For example, Alq_3 can act both as the EML [21, 23] and ETL [23], NPD can be either the EML [24] or HTL [25], and CBP can be used as either the EML [20] or host material [26].

Conventional OLEDs are mostly bottom emitting, in which the light is emitted from the transparent substrate and semi-transparent bottom anode, i.e. light is extracted from the thin film transistor (TFT) substrate side. Most bottom-emitting OLEDs utilize a glass/ITO substrate, with the organic layers grown layer-by-layer on top of the substrate using the thermal vacuum deposition technique. In contrast to bottom-emitting OLEDs, an inverted OLED has a bottom cathode which can be connected to the drain of a TFT used in active matrix OLED displays [27]. Inverted OLEDs can be either bottom or top emitting.

1.4 Working principle of phosphorescent OLEDs

As shown in the figure 1.5, during operation, a voltage is applied across the cathode and anode, as a result electrons are injected from the cathode into the lowest unoccupied molecular orbital (LUMO) of the ETL and holes are injected from the anode into the highest occupied molecular orbital (HOMO) of the HTL. The electrons and holes then move towards the emission layer under the influence of the applied electric field. Some of these carriers form excitons within the EML. Excitons are normally confined in the EML by the HTL and ETL which also function as charge blocking layers. The radiative recombination of the excitons leads to light emission. This is the basic principle of OLED operation. The emitted photon energy depends on the bandgap of the emitter - the difference in the energy between the HOMO and the LUMO of the EML material.

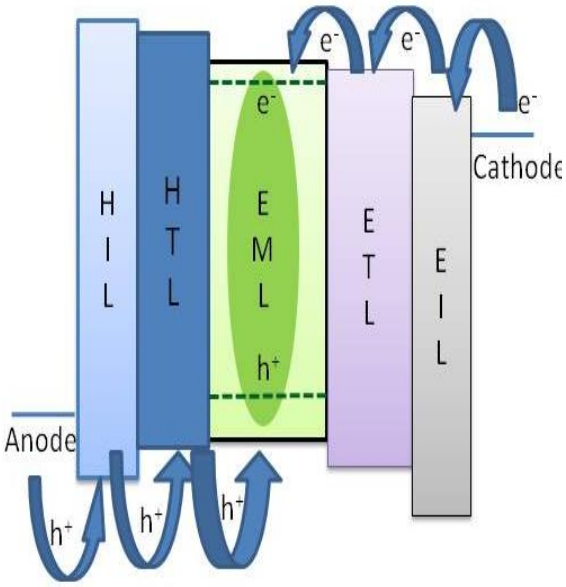

Figure 1.5 Schematic showing working principle of a PhOLED

In phosphorescent devices, some of the excited triplet excitons are lost by triplet-triplet annihilation. The triplets with energy T_1, collide and thus the energy is transferred to other excited states, therefore the phosphorescence in quenched. Because of this reason, emission layer in the PhOLEDs are prepared by doping a small amount of phosphorescent material into a host material that acts as a buffer layer between the phosphorescent complexes [28]. Therefore, it is critical, that the energy from the host material is transferred to the guest (phosphorescent) material, for efficient radiative emission.

Since, EML of PhOLED consists of phosphorescent molecules doped in a suitable host material the process of exciton generation; recombination and light emission is more complicated. Excitation energy from the host molecule is transferred to the phosphorescent guest molecule [29] and is explained by two processes – Forster energy transfer and Dexter energy transfer.

Forster energy transfer mechanism, also called as Coulomb mechanism is the interaction between the electrical dipoles. The energy transfer probability is proportional to R^{-6}, where R is the distance between the interacting species. Since, spin conversion is required in this type of interaction; usually single excitons are involved in Forster mechanism.

Dexter energy transfer mechanism is purely quantum mechanical and requires the overlap of molecular orbitals in which the energy transfer occurs. The interaction occurs for both the spin conservation and spin transfer between molecules, meaning for both the singlet and triplet exciton energy transfer. Therefore, dexter mechanism is the dominant is host-guest system such as CBP:$Ir(ppy)_3$.

Also it is crucial that the host material has good charge transport abilities, and is even more important to have both the singlet and triplet energy level of the host material higher than the triplet state of the phosphorescent dopant material in order to have efficient energy transfer.

1.5 OLEDs Fabrication

In general, there are two broad classes of π-conjugated materials, polymers and small molecules. A polymer is composed of *n* number of repeating units ($n>>1$), called as monomers, and is considerably macromolecule having a higher molecular weight. Small molecules lack repeating units and are thus smaller units having lower molecular weights. Accordingly, OLEDs are also classified as small molecule OLEDs (SMOLEDs) and polymer OLEDs (PLEDs). SMOLEDs are fabricated using thermal evaporation in a vacuum. The generally low melting points of small molecules allow deposition of controlled and homogenous films in the vacuum and ease the process of multilayer deposition. However, high vacuum ($<10^{-6}$ torrs) demands for

expensive and complex fabrication set up, and such vacuum deposition instruments set limits on the device size [30-31].

Polymers tend to decompose or crosslink at higher temperatures, therefore thermal evaporation is not a good choice. PLEDs are fabricated by solution processing techniques, such as spin-coating, inkjet printing and screen printing. This allows fabricating large area and cost effective PLEDs [31-32]. Solution processing is a simple and cost effective, but in order to fabricate complex multilayered structure PLEDs; it requires multiple orthogonal organic solvents and has its limitations [33].

OLED materials are highly sensitive to ambient conditions, including water and oxygen species. The as-fabricated devices must be encapsulated in an inert ambient (e.g., a glovebox attached to the deposition system). After encapsulation, the performance of OLEDs can be characterized by measuring the following characteristics.

1.5.1 OLEDs figure of Merit

Internal Quantum Efficiency (IQE)

The internal quantum efficiency (η_{int}) is defined as the ratio of the total number of photons generated within the device to the total number of charges injected, and mathematically expressed as,

$$\eta_{int} = \gamma \eta_{exc} \varphi_P$$

where γ is the electron-hole charge balance factor (~ 1), η_{exc} is fraction of excitons formed within

the EML that results in radiative decay (η_{exc} = 0.25 in fluorescent emitters and 1 in phosphorescent emitters), and φ_{PL} is the intrinsic quantum efficiency for radiative decay [34, 35].

External Quantum Efficiency (EQE)

The external quantum efficiency η_{ext} is defined as the ratio of the total number of photons emitted by the OLED into the air to the total number of charges injected and mathematically expressed as [34, 35],

$$\eta_{ext} = \eta_{int}\, \eta_{coupling}$$

where, $\eta_{coupling}$ is the light outcoupling efficiency, i.e. the fraction of photons which can escape from the device. It depends on the refractive index of the layers and geometry of the device. For typical OLEDs on glass without outcoupling enhancement, $\eta_{coupling}$ is about 20.

Current Efficiency

Since most OLEDs emit in the visible spectrum, the photopic response, also called human eye response, directly affects the luminous efficiency of the device. The luminous efficiency η_L in candela per amperes (Cd/A) is equivalent to η_{ext} , with an exception that η_L weights the photons according to the photopic response of the eye. Mathematically, η_L is defined as,

$$\eta_L = L/J$$

where, *L* is the brightness in Cd/m^2 and *J* is the current density in A/m^2 of the OLEDs.

Power Efficiency

Another commonly used efficiency is the power efficiency η_p, in lumens per watt (lm/W). It is the ratio of the luminous power emitted by the device, L_p (lm) to the total electrical power required to drive the OLEDs at a particular voltage (*V)*.

Lifetime

Lifetime of an OLED is essential for commercial applications. A decrease in brightness of OLED is observed over time due to various mechanisms such as device and/or material degradation etc. The half-lifetime is common term to express the device's operational lifetime, and is defined as the time it takes for an OLED to show half of the initial brightness under the constant current of constant voltage operation.

Color Purity

It is critical for an OLED to achieve wide color gamut for display applications. Therefore, three primary colors red, green and blue (RGB) should be as pure as possible. Meaning, the emission spectrum should be as narrow as possible to approximate monochromatic emission. For an optimized gamut, monochromatic wavelengths required for RGB are 700 nm, 546.1 nm and 435.8 nm respectively.

1.5.2 OLEDs performance measurement

Current-voltage (IV) measurement

Current-voltage measurements were made using an Agilent 4156 C semiconductor parameter analyzer, where the current was measured as a function of the applied voltage. The

test set up was connected to a computer where the software was used to control the testing parameters.

Electroluminescence (EL) spectra measurements

The OLEDs were injected with the current in the range of 10-5 to 10-2 A by a Keithley sourcemeter and the emission spectra were recorded using an Ocean Optics spectrometer.

Luminance measurement

Luminance meter was used to measure the value of luminance of the OLED as a function of applied current or voltage. The meter would give direct value of luminance in cd/m^2.

External quantum efficiency (EQE) measurement

The device was placed on top of calibrated silicon photodiode and was swept with voltage from a Keithley sourcemeter. All the emitted photons were then captured by the photodetector and were converted into photocurrent. Simultaneously, current-voltage and photocurrent-voltage were measured with the set up.

EQE value was obtained by dividing the photocurrent values by current values at various ranges of voltages, i.e., (Photocurrent / Current).

Current efficiency

Current efficiency (Cd/A) at a particular voltage, V were calculated using,

$$= \text{Luminance } (Cd/m^2) \text{ at V} / \text{ Current density } (A/m^2) \text{ at V}$$

Power efficiency

Power efficiency, (lm/W) at a particular voltage, V were calculated using,

= Current efficiency (Cd/A)/Voltage (V)

1.6 Challenges facing phosphorescent OLEDs (PhOLEDs)

Although PhOLEDs with nearly 100% internal quantum efficiency are drawing increasing attention for practical applications due to the following factors - self emitting property, high luminescence efficiency, broad wavelength range, wide viewing angle, high contrast, low power consumption, low weight, and large emitting area [36] - there are still many challenges needed to be addressed. Current manufacturing process steps used to fabricate PhOLEDs are expensive and limited to small size devices [37-39]. Low intrinsic conductivity in organic materials and their poor stability directly affect the efficiency and lifetime of the devices, causing slow market penetration and limiting the competitiveness of OLEDs compared to other types of emitters [40]. The biggest technical challenge is the limited lifetime of the device [41]. Sensitivity of the organic materials used in device fabrication to the environment (oxygen and moisture) degrades the device over time, and thus limits their efficiency and lifetime.

To develop efficient and reliable OLEDs, significant current research efforts focus on performance enhancement of PhOLEDs through structure optimization. Since, organic semiconductor materials generally lack intrinsic charge carriers because of weak intermolecular coupling – one has to look for ways to increase the extrinsic carrier concentration by current injection. This can be achieved by using materials with better charge injection and better charge transport abilities. Out of various approaches used, one is to insert thin interlayer which facilitate

charge injection into charge transport layers, and use materials with higher intrinsic conductivities for more facile charge transport. Inorganic semiconductors have been so far promising in this context, since these materials have higher conductivity values in addition to better stability compared to organic materials. Various Metal oxide semiconductors have been are so far most popular and convincing inorganic materials used as charge injecting layers in the OLED structure [50]. The popularity of metal oxide semiconductors lies in their variety, chemical stability, and physical properties such as transparency, low toxicity, high charge mobilities and inexpensiveness [50]. Thin films (<2 nm) of different metal oxides have been incorporated in OLEDs to enhance hole injection, including yttrium oxide, terbium oxide, titanium oxide, zinc oxide, niobium oxide, gallium oxide, tin oxide [42]. Similarly, on the cathode side, insulating metal oxides like aluminum oxide, magnesium oxide, and silicon oxide have been inserted between the aluminum cathode and the organic layer to increase the electron injection efficiency. [43-47]. Better device performance due to improved charge injection in these above cases has been attributed to the modification of the energy band structure at the electrode/organic layer interfaces by the thin oxide layer. As a voltage drops across the oxide layer, the field tilts the energy levels, lowering the energy barriers for charge injection. This has been supported by investigations through photoelectron spectroscopic measurements.

It has been successfully demonstrated that metal oxide charge injection layers can dramatically improve the device stability and lifetime due to more efficient and balanced charge injection [48, 49]. It is also due to the fact that metal oxides are thermal stable, creating robust inorganic interfaces. Hybrid inorganic organic light emitting diodes (HyLEDs) with inorganic materials playing more roles are therefore of high practical interest as they tend to addresses challenges facing current OLEDs pertaining the device lifetime.

1.7 Goals and Scope of Thesis

The goal of this thesis is to develop hybrid inorganic-organic light emitting diodes (HyLEDs) with inorganic charge injection and transport layers, which exhibit improved luminous efficiency and operational lifetime as compared to all-organic OLEDs. In an attempt to achieve this goal, we preformed the following works in sequence:

First, thin films of zinc-tin-oxide (ZTO) and tungsten oxide (WO_3) were prepared on glass substrates using thermal vacuum evaporation and characterized. Separate sources of zinc oxide and tin oxide were co-evaporated and ZTO films of various compositions (at.%Zn from 0-100%) were prepared. The ZTO films were then treated in rapid thermal annealer (RTA) at various temperatures in oxygen atmosphere. Finally, morphological, structural, optical and electrical properties were identified and studied. The goal of this work was to evaluate the application of ZTO thin films as a transparent electrode and ETL in optoelectronic devices. We also prepared WO_3 thin films using thermal vacuum evaporation and studied its optical, electrical properties. The goal was to use thin films of WO_3 films as the HTL in PhOLEDs. This is detailed in chapter 2 of the thesis.

Second, we fabricated HyLEDs based on hybrid heterostructure comprises different metal oxides. HyLEDs with MoO_3 injection layer, WO_3 hole transport layer, ZTO electron injection layer were fabricated and characterized. The Device structure was optimized to obtain high efficiency and long operational lifetime. We successfully developed HyLEDs based on a simplified hybrid structure with a WO_3 HTL, and achieved significant performance enhancement over all-organic PhOLEDs. This work is detailed in chapter 3.

Finally, we fabricated and characterized inverted HyLEDs having a WO_3 HTL. Different metals including Ca, Ca/LiF, and Al/LiF have been evaluated as the cathode of the inverted devices, and their impact on electron injection was studied. It has been found that using the WO_3 HTL in conjunction with a nanometer-thick Ca cathode resulted in balanced charge injection, and thus inverted HyLEDs with good luminous efficiency and reliability. This work is detailed in chapter 4.

References

[1] Destriau, G. AC electroluminescence in ZnS. J. Chim. Phys. 33, 587 (1936).

[2] M. Pope, H. P Kallmann, and P. Magnante, J.Chem. Phys. 38, 2042 (1963); M.Sano, M.Pope, and H. Kallman, J. Chem. Phys. 43, 2920 (1965)

[3] W. Helfrich and W. G. Schneider, Phys. Rev. Lett. 14, 229 (1965); W. Helfrich and W.G. Schneider, J. Chem. Phys. 44, 2902 (1965)

[4] P. S. Vincentt, W. A. Barlow, R. A. Hann, and G. G. Roberts, Thin Solid Films 94, 171 (1982)

[5] R. Partridge, Polymer 24, 733 (1983).

[6] R. Partridge, Polymer 24, 739 (1983).

[7] R. Partridge, Polymer 24, 748 (1983).

[8] R. Partridge, Polymer 24, 755 (1983).

[9] C. W. Tang and S. A. VanSlyke, Appl. Phys. Lett. 51, 913 (1987)

[10] J. H. Burroughes, D. D. C. Bradley, A. R. Brown, R. N. Marks, K. MacKay, R. H. Friend, P. L. Burns and A. B. Holmes, Nature 347, 539 (1990).

[11] M. A. Baldo, D. F. O'Brien, Y. You, A. Shoustikov, S. Sibley, M. E. Thompson and S. R. Forrest, Nature 395, 151 (1998).

[12] C. K. Chiang, C. R. Fincher, Y. W. Park, A. J. Heeger, H. Shirakawa, E. J. Louis, S. C. Gau, and A. G. MacDiarmid, Electrical Conductivity in Doped Polyacetylene, Phys. Rev. Lett. 39, 1098-1101 (1977).

[13] Abay Gadisa, Studies of charge transport and energy levels in solar cells based on polymer/fullerene bulk heterojunction; Linkoping Studies in Science and Technology Dissertation No. 1056

[14] C. Jacko, Ross H. McKenzie and B.J. Powell, J. Mater. Chem. 2010, 20, 10301-10307

[15] C. W. Tang and S. A. VanSlyke, Appl. Phys. Lett. 51, 913 (1987).

[16] C. Adachi, M. A. Baldo, M. E. Thompson and S. R. Forrest, J. Appl. Phys. 90, 5048 (2001).

[17] M. A. Baldo, S. Lamansky, P. E. Burrows, M. E. Thompson and S. R. Forrest, Appl. Phys. Lett. 75, 4 (1999)

[18] X. Yang, D. Neher, D. Hertel and T. Daubler, Adv. Mater. 16, 161 (2004).

[19] D. F. O'Brien, M. A. Baldo, M. E. Thompson and S. R. Forrest, Appl. Phys. Lett. 74, 442 (1999).

[20] L. Zou, V. Savvate'ev, J. Booher, C.-H. Kim and J. Shinar, Appl. Phys. Lett. 79, 2282 (2001).

[21] Z. Gan, Y. Tian, D. W. Lynch, J-H. Kang, Q-H. Park and J. Shinar, J. Appl. Phys. 106, 094502 (2009).

[22] K. O. Choen and J. Shinar, Appl. Phys. Lett. 81, 1783 (2002).

[23] G. Xie, Y. Meng, F. Wu, C. Tao, D. Zhang, M. Liu, Q. Xue, W. Chen and Y. Zhao, Appl. Phys. Lett. 92, 093305 (2008).

[24] H. Mu, I. Reddy, J. Hunt, P. Severs and S. Patil, J. Phys. D: Appl. Phys. 43 195103 (2010)

[25] Y. Zheng, S-H. Eom, N. Chopra, J. Lee, F. So, and J. Xue, Appl. Phys. Lett. 92, 223301 (2008).

[26] Z. B. Wang, M. G. Helander, J. Qiu, D. P. Puzzo, M. T. Greiner, Z. W. Liu and Z.H. Lu, Appl. Phys. Lett. 98, 073310 (2011).

[27] T.-Y. Chu, J.-F. Chen, S.-Y. Chen, C.-J. Chen and C. H. Chen, Appl. Phys. Lett. 89, 053503 (2006).

[28] A. Quan, F. Teng , Z. Xu , D. Wang , S. Yang , Y. Hou , Y. Wang , Phys.Lett. A 2006, 352, 434.

[29] Yang, X.; Neher, D. Polymer Electrophosphorescence Devices. In Organic Light-Emitting Devices; Müllen, K., Scherf, U., Eds.; Wiley-VCH: Weinheim, 2006; p. 333.

[30] B.W. D'Andrade, M.E. Thompson and S.R. Forrest, Adv. Mater. 14, 147 (2002).

[31] M. C. Gather, A. Köhnen and K. Meerholz, Adv. Mater. 23, 2 (2011).

[32] J. Huang, G. Li, E. Wu, Q. Xu and Y. Yang, Adv. Mater. 18, 114 (2006).

[33] S.R. Forrest, Nature 428, 911 (2004).

[34] S. R. Forrest, D. D. C. Bradley and M. E. Thompson, Adv. Mater. 15, 1043, 2003

[35] K. Saxena, V. K. Jain and D. S. Mehta, Opt. Mater. 32, 221 (2009).

[36] Bernard Geffroy, Philippe le Roy, and Christophe Prat. Polym Int 55:572–582 (2006)

[37] C. Adachi, M. A. Baldo, S. R. Forrest and M. E. Thompson, Appl. Phys. Lett. 77, 904 (2000).

[38] J. S. Huang, M. Pfeiffer, A. Werner, J. Blochwitz, K. Leo and S. Y. Liu, Appl.Phys. Lett. 80, 139 (2002).

[39] B.W. D'Andrade, M.E. Thompson and S.R. Forrest, Adv. Mater. 14, 147 (2002).

[40] Michele Sessolo and Henk J. Bolink, Adv. Mater. 2011, 23, 1829–1845

[41] "OLED TV estimated lifespan shorter then (sic) expected", www.hdtvinfo.eu.

[42] J. L. G. Fierro, Metal Oxides–Chemistry and Applications, CRC Press, Taylor & Francis Group, 2006.

[43] F. Li, H. Tang, J. Anderegg, J. Shinar, Appl. Phys. Lett. 1997,70,1233.

[44] H. Tang, F. Li, J. Shinar, Appl. Phys. Lett. 1997, 71 , 2560.

[45] H. W. Choi, S. Y. Kim, W.-K. Kim, J.-L. Lee, Appl. Phys. Lett. 2005, 87,082102.

[46] H. W. Choi, S. Y. Kim,W.-K. Kim, K. Hong, J.-L. Lee, Appl. Phys.Lett. 2006,100, 064106.

[47] A. Quan, F. Teng, Z. Xu, D. Wang, S. Yang, Y. Hou, Y. Wang, Phys.Lett. 352- 434 (2006).

[48] Michele Sessolo and Henk J. BolinkAdv. Mater. 23, 1829–1845 (2011).

[49] H. J. Bolink, H. Brine, E. Coronadoa and M. Sessolo, J. Mater. Chem., 20, 4047–4049 (2010).

Chapter 2

Thermal evaporation and characterization of metal oxide thin films

2.1 Zinc-tin-oxide (ZTO)

2.1.1 Introduction

Transparent conducting oxides (TCOs) have been extensively used as transparent electrodes for flat-panel displays, solar cells, gas sensors, and light-emitting diodes [1-7]. Zinc-tin-oxide (ZTO) materials, among many TCOs, recently attracted much attention due to their good thermal and chemical stability [1-5]. Unlike other popular TCOs such as In-Sn-O (ITO) and Cd-Sn-O (CTO), ZTO films do not contain expensive or toxic elements, and thus are cheaper and more environmentally benign. ZTO films are usually deposited by sputtering [8-11], pulsed laser deposition (PLD) [12], filtered vacuum arc [13], and flash evaporation [14]. The growth kinetics seems to have a significant impact on the structure and properties of ZTO films [8-14]. Thermal evaporation, however, has not been explored as an alternative approach for ZTO deposition. In some cases, it would be desirable to deposit ZTO films in a thermal evaporator. For example, in many organic and hybrid devices [4, 5], ZTO may be used as the cathode or electron transport layer. If the ZTO layer is deposited by thermal evaporation, the entire device structure may be fabricated in one system without breaking the vacuum.

In this section, we present a study of the structural, electrical and optical properties of ZTO films deposited on glass using thermal co-evaporation. The properties are studied as a function of the composition which is varied by changing the atomic percentage, (at. %) of Sn from 0 - 1. Furthermore, the effects of post-annealing in air on the ZTO properties are also

investigated. Since evaporated ZTO films exhibit n-type conductivity, they may be used as electron injection and transport layers in hybrid LED structures.

2.1.2 Thermal co-evaporation deposition of zinc-tin-oxide (ZTO) films

ZTO thin films were prepared using vacuum thermal evaporation process. 100 nm-thick ZTO thin films were deposited on clean glass substrates by thermal co-evaporation of ZnO (powder) and SnO_2 pellets from two separate crucibles in a multi-source vacuum deposition system. The system base pressure was ~1×10^{-7} torr, and the pressure stayed at ~1×10^{-6} torr during the deposition. The experiment was repeated under similar conditions by varying the ratio of ZnO and SnO_2 fluxes in order to prepare SnO_2, ZnO, and ZTO films with the at.% Sn (which is defined as the ratio of Sn/Sn+Zn) of 0.25, 0.33, 0.5, 0.67, and 0.75. The atomic ratios were calculated based on the ratios of the deposition rates of ZnO and SnO_2. The ratios were confirmed with the results measured by energy dispersive X-ray spectroscopy (EDX). Samples of each ratio of ZTO thin films were annealed in air at 150 - 550 ^{o}C for 20 min. The as-deposited and annealed thin films were characterized by atomic force microscopy (AFM) and X-ray diffraction (XRD) for surface and morphology studies. The optical characterization was performed measuring the transmission spectrum using a Hitachi U-3900H UV-Vis spectrophotometer. The sheet resistances of the films were determined using the four-point probe technique, and then converted into electrical resistivity.

2.1.3 Surface and Structural Characterization

Figure 2.1 shows the surface morphology of the films examined by AFM with 5×5 μm^2 scans of the as-deposited SnO_2, ZnO and ZTO with 25, 50 and 75 at.% Sn. The pristine ZnO and

SnO_2 were relatively smooth and uniform whereas, the ZTO films were significantly rougher and composed of larger grains on the order of hundreds of nanometers.

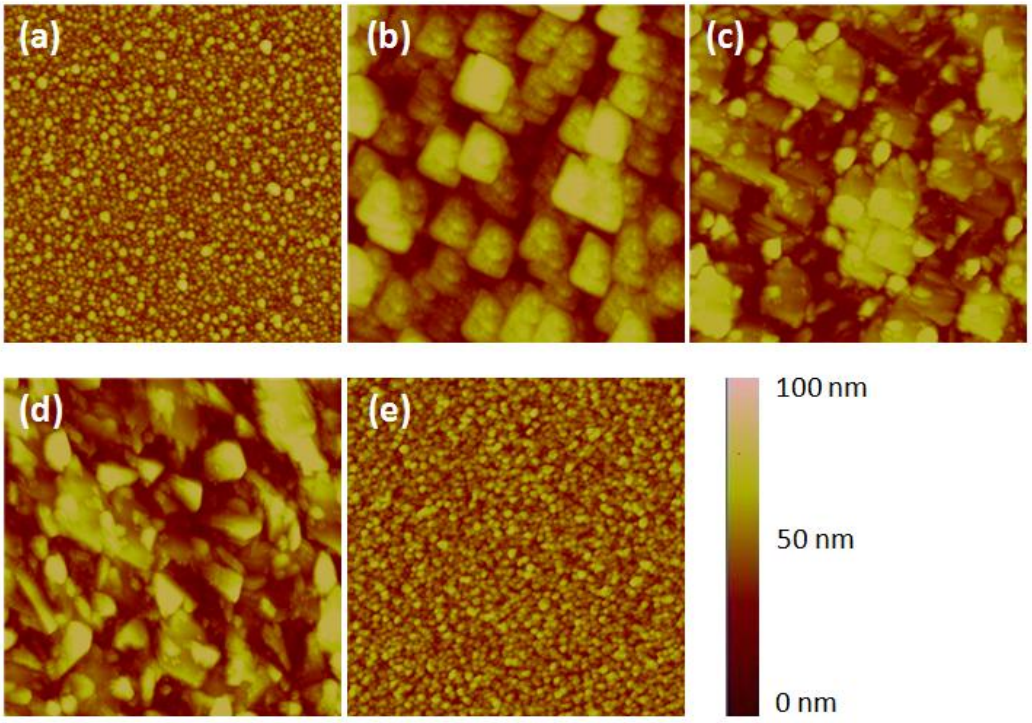

Figure 2.1 5×5 μm^2 AFM micrographs of 100 nm as-deposited (a) ZnO, (b) ZTO with 25at.% Sn, (b) ZTO with 50at.% Sn, (b) ZTO with 75at.% Sn, (b) SnO_2 films.

Also seen from the figure 2.2 is the rms roughness value of ZTO with 50at. % Sn increases with increasing annealing temperature. As seen, the roughness of the as-deposited ZTO increases and then decreases with increasing Sn content. The rms values ranging from 26-36 nm are larger than those of typical sputter-deposited films [9]. This may be attributed to more directional growth under lower processing pressure as well as lower adatom mobility due to less energetic evaporated species compared to sputter-ejected species. The surface roughness of the

ZTO with 50at. % Sn increases slightly after annealing, indicating the growth of the grain size as a result of coalition of smaller grains.

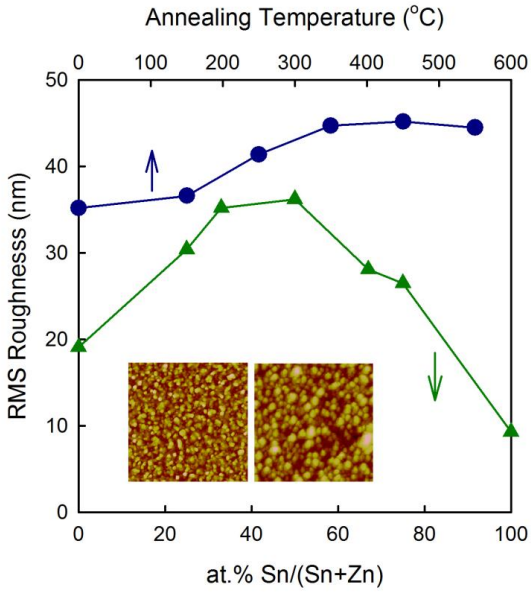

Figure 2.2 RMS roughnesses of as-deposited ZTO films as a function of Sn content and of ZTO with 50at. % Sn

XRD scans of both the as-deposited and the annealed 33at% ZTO films are shown in Figure 2.3 below. Small halos around $2\theta = 30^{o}$ for 550 ^{o}C annealed ZTO indicated the amorphous nature of the films. Similar results were obtained from thicker films (~175nm) deposited on Si (100) substrates and other ZTO compositions suggesting that the grains revealed by AFM in Fig. 2.1 are more likely amorphous particles. This result is consistent with the result of sputter-deposited ZTO films [9], which showed ZTO sputter-deposited at room temperature remained amorphous after annealing below 600 ^{o}C. Whereas, the ZTO films deposited by PLD were found to be crystallized upon annealing at 450 ^{o}C [12] this is attributed to higher precursor energies of the depositing species. With the advantage of low processing temperature of thermal

evaporation, amorphous ZTO films may be grown on plastic substrates, and are attractive for easy integration with organic and nanocrystal materials for practical device applications.

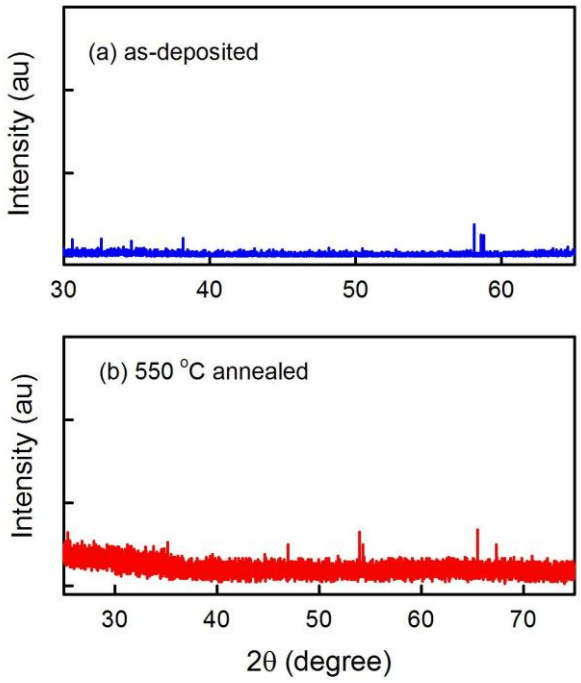

Figure 2.3 XRD scans of 33at% ZTO films (a) as-deposited and (b) 550 ^{o}C annealed

2.1.4 Electrical Characterization

The resistivity of ZnO, SnO_2, and ZTO films annealed in air at different temperatures is shown in Figure 2.4. As seen from the figure, the dependence of the resistivity of ZnO and ZTO films on post-annealing temperature follows the same trend. The resistivity shows small changes below 250 ^{o}C, increases rapidly from 250 - 450 ^{o}C by as much as six orders of magnitude, and saturates or decreases slightly after 550 ^{o}C annealing. Also, to be noted that the SnO_2 film exhibits a little different behavior, indicating its relatively poor thermal stability. Its initial resistivity is two orders of magnitude higher than the other composition films. The value drops

down at 150 ^{o}C and increases rapidly until annealing at 350 ^{o}C and then drops quickly beyond 350 ^{o}C.

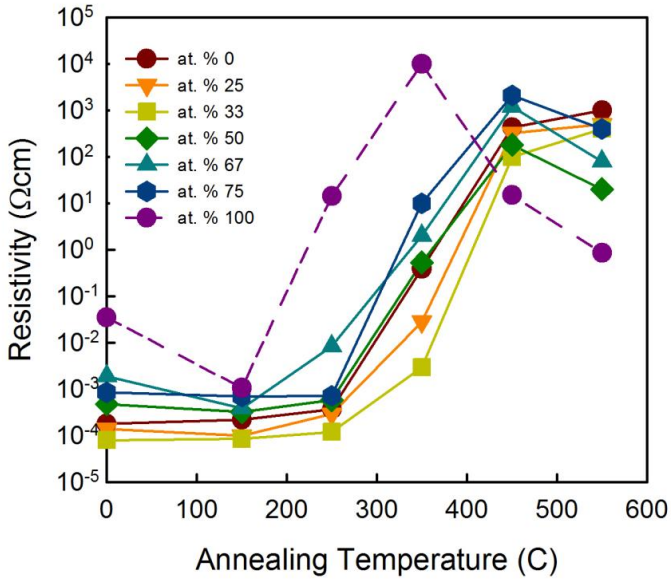

Figure 2.4 Resistivity of ZnO, SnO_2, and ZTO with different Sn contents as a function of post-annealing temperature.

Since all the films remain amorphous, substantial changes in the electron mobility are not expected. Thus, the resistivity variations can be attributed from the changes in the electron concentrations within the ZTO composition. As a matter of fact, vacuum deposited ZnO and SnO_2 films using thermal evaporation are non-stoichiometric due to oxygen deficiency. This has been observed using X-ray photoelectron spectroscopy, energy dispersive X-ray spectroscopy, and Rutherford backscattering spectrometry [12, 14-16] by other researchers.

Oxygen vacancies have been found to act as donor states in the ZTO films [8-14], thereby increasing the electron concentration. As a consequence the remarkable increase in resistivity upon annealing from 250 - 450 ^{o}C is solely attributed to increased oxygen incorporation. This is

due to a reduced density of oxygen vacancies and subsequently reduced electron concentration. The resistivity values of the as-deposited ZTOs with different compositions are in the range of 10^{-5}-10^{-3} Ωcm, which are much lower than those of ZTO films deposited by other techniques [8-14]. It is plausible that ZTO deposited by thermal evaporation in vacuum contains a higher density of oxygen vacancies.

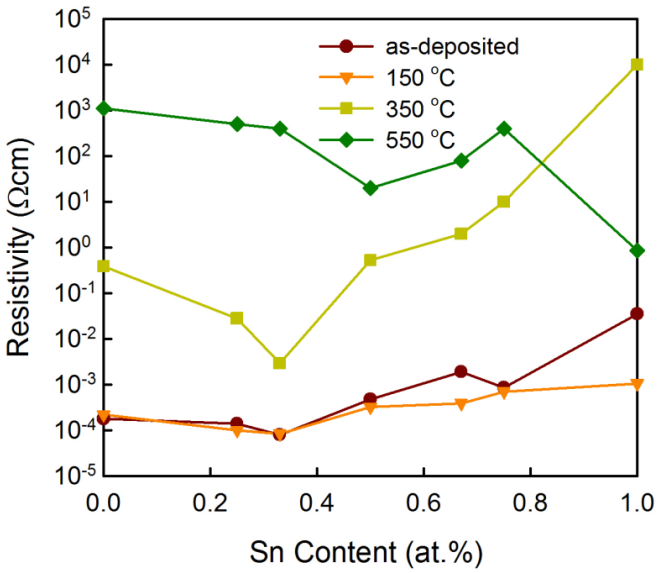

Figure 2.5 Resistivity variations with Sn atomic concentration for as-deposited and annealed ZTO films

Also we investigated the resistivity variations with the ZTO composition for the as-deposited and annealed samples. As seen from the Figure 2.5, increasing Sn content has the effect of decrease in resistivity at first and then increase in it. Increase in Sn atomic concentration into the ZnO matrix may create an additional donor states due to the lower electronegativity of Sn than of Zn. This leads to enhanced conductivity [14]. As a consequence, for the as-deposited film and ZTO annealed below 350 ^{o}C, the resistivity reaches the minimum at 33at. % Sn.

However, for the 550 ^{o}C annealed ZTO the lowest resistivity was at 50at. % Sn. Another interesting feature in Fig. 2.1.5 is that below 550 ^{o}C, the ZTO films with low Sn content have lower resistivity than the ZTO with high Sn content. It is perceived that the predominant local structure of the former is the mixture of ZnO and Zn_2SnO_4, whereas the latter is mainly composed of SnO_2 and $ZnSnO_3$ phases [10-12], so our finding is opposite to what was found in work of ref. 11, which showed that Sn-rich phases were more conductive than Zn-rich phases in sputter-deposited films. A possible explanation for this discrepancy is that more ZnO is reduced to metal Zn during the evaporation due to a much higher melting temperature of ZnO than SnO_2, leading to a higher density of oxygen vacancies in Zn-rich ZTO.

2.1.5 Optical Characterization

The as-deposited films of all the compositions appeared to be gray and metallic. Because it is believed that a significant amount of these metal oxides were reduced to metal Zn and Sn during the evaporation. The films became more transparent upon annealing in air at increasing temperature. Figure 2.6 shows the transmission spectra of ZTO with 25at. % and 75at. % Sn after annealing from 150 to 550 ^{o}C. As seen from the transmission spectrum, annealing above 350 ^{o}C results in substantial increase in transparency. This is attributed to re-oxidation of the reduced metals during annealing in air process. This is supported by the fact that similar samples annealed in ambient N_2 at the same temperatures are much less transparent.

Also seen, after 550 ^{o}C annealing, the transmission of the film is greater than 80% in much of the visible spectrum. Also seen is the absorption edges of these two materials are similar and nearly independent of the annealing temperature. The absence of the Bernstein-Moss effects, which have been seen in sputter-deposited ZTO as blue-shifts of the absorption edge with

increasing annealing temperature [9-11], confirms small structural changes in the evaporated ZTO films during annealing.

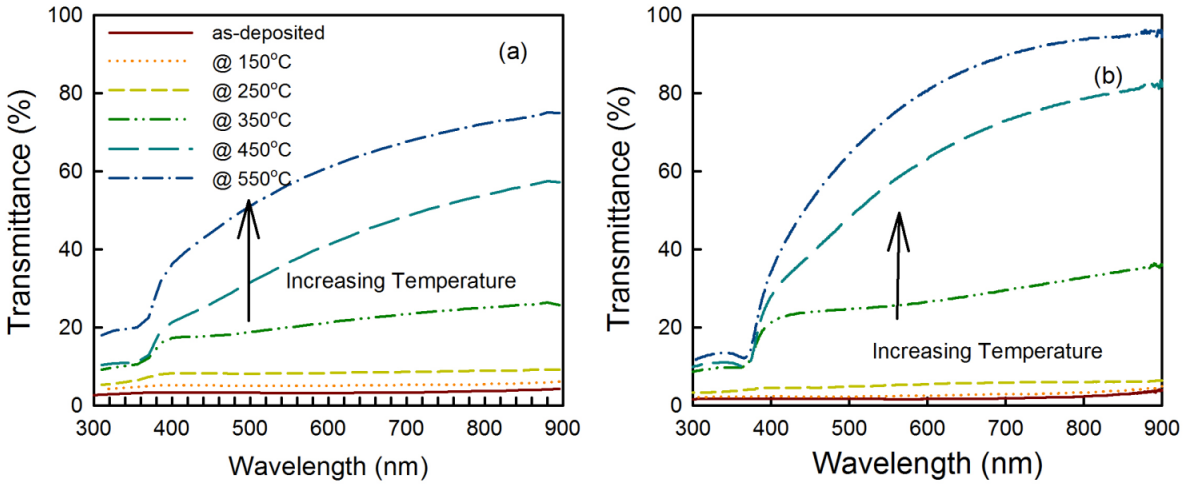

Figure 2.6 Transmission spectra of ZTO with (a) 25at. % Sn and (b) 75at.% Sn annealed in air

Figure 2.7 below shows the variations of the optical transmission at 530 nm for all the samples with post-annealing temperature. Except for SnO_2, which becomes transparent after annealing at 250 ^{o}C, all other samples start becoming transparent only after 350 ^{o}C.

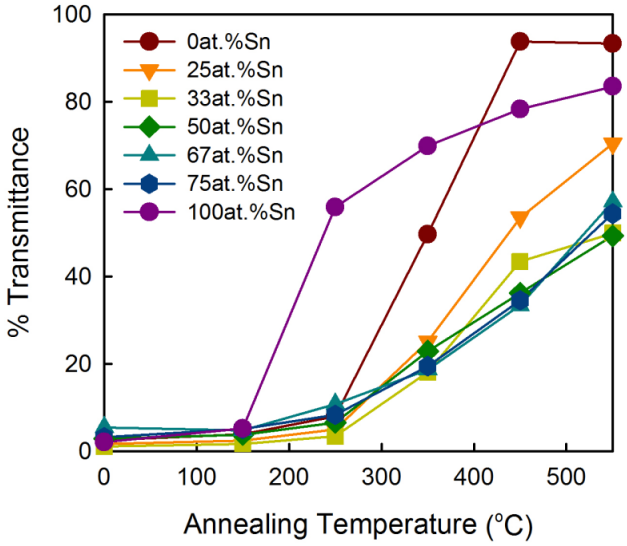

Figure 2.7 Transmission spectra at 530 nm of ZnO, SnO_2, and ZTO with different Sn contents, as a function of post-annealing temperature.

The transmission of all ZTO films increases nearly linearly with increasing temperature, however it is still below 70% after 550 ^{o}C annealing. Whereas, the ZnO and SnO_2 films were 93% and 84% transparent after 550 ^{o}C annealing at 530 nm, respectively. The trends show that the transmission evolution of the film is accompanied by the increase in resistivity. It is clear that a trade-off exists between optical transparency and electrical conductivity for annealed ZTO films. So, in cases where transparency is a more important criterion than conductivity, the films should be annealed at a higher temperature and vice versa. In addition, the transparency of the films may also be improved by introducing oxygen plasma into the vacuum chamber during the deposition process [8].

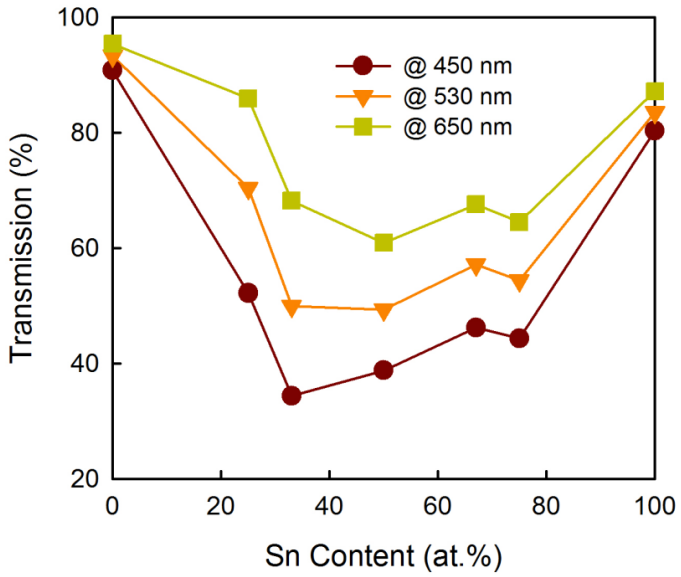

Figure 2.8 Transmission of 550 ^{o}C annealed ZTO films at red, green and blue wavelengths, as a function of Sn content.

Figure 2.8 above, shows the transmission spectra of 550 ^{o}C annealed ZTO films, measured at red (630 nm), green (530 nm) and blue (450 nm) wavelengths, as a function of Sn content. As observed, that pure ZnO and SnO_2 films are more transparent than the ZTOs. This may be attributed to light scattering by domain boundaries and the larger grain sizes as seen from AFM images in the ZTO films than in pure ZnO and SnO_2 films. Among the ZTO films, the film with 25 at.% Sn has the highest transmission, indicating that with less Sn incorporated into the ZnO matrix, the film contains a lesser amount of mixing phases thus a lower number of scattering defects.

We also investigated how the absorption edge evolves in the various compositions ZTO films, the transmission spectra of all the samples annealed at 550 ^{o}C were plotted as shown in

Figure 2.9. ZnO and SnO_2 have absorption edges at ~369 nm (corresponding to 3.36 eV) and ~337 nm (corresponding to 3.68 eV), respectively.

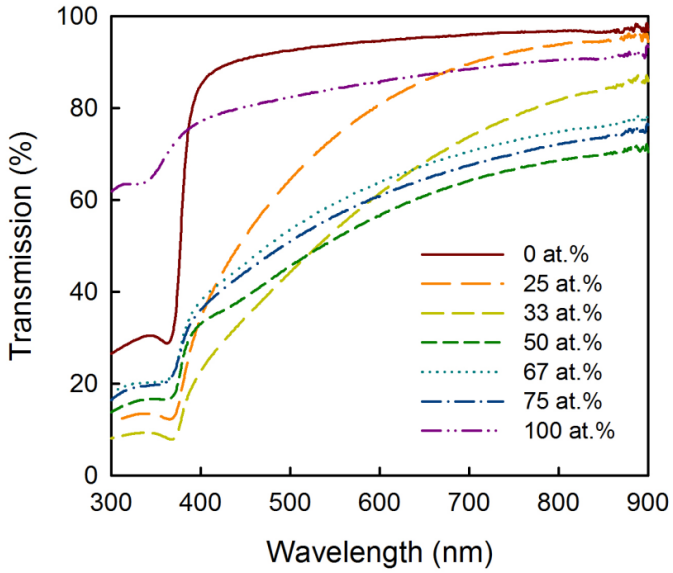

Figure 2.9 Transmission spectra of ZnO, SnO_2, and ZTO films with different Sn contents, all annealed at 550 ^{o}C in air for 20 min.

This estimation is consistent with that fact that their energy band gaps are 3.4 eV (ZnO) and 3.7 eV (SnO_2). Interestingly, the absorption edge of ZTO films showed little dependence on its composition as seen from the figure, corresponding close to the absorption edge as of pure ZnO film. The result implicates that the local structure of the ZTO films is dominated by separate ZnO and SnO_2 phases instead of a Zn-O-Sn phase. Similar observation was found on ZTO films deposited by flash evaporation [14], concluding that the absorption edge of ZTO is mainly determined by that of the smaller band gap material, ZnO.

2.2 Thermal evaporation and characterization of WO_3 thin films

2.2.1 Introduction

Transition metal oxides (TMOs) have been extensively used in electronic, magnetic and other applications [17, 18]. TMOs thin films prepared by various methods shows excellent properties including environmental stability, optical transparency in the visible range, mechanical robustness and good charge transport properties [19-21]. TMOs such as MoO_3, WO_3, V_2O_5 have been recently demonstrated as efficient hole injection layers in organic LEDs [21-28] and solar cells [30]. It has been demonstrated that the evaporated thin films of WO_3 is inherently p-type in nature [29-31] and has a low lying valence band. Therefore, it may also be used as a hole transport material in various optoelectronic devices. In this section, we will study the morphological, optical and electrical properties of thermally evaporated WO_3 thin films and evaluate their applicability as hole injection and/or transport layers in HyLEDs.

2.2.2 Evaporation deposition of WO_3

100 nm thick WO_3 thin films of were prepared by thermal evaporation using a source of tungsten oxide pellets (99.9% purity) on clean glass substrates. The system base pressure was $\sim 1\times10^{-7}$ torr, and the pressure stayed at $\sim 1\times10^{-6}$ torr during the deposition. The films were annealed in a rapid thermal annealing (RTA) system at various temperatures in the air for 20 minutes. Surface morphology of the films was studied by using atomic force microscopy (AFM). Their optical transmission spectra were measured using a Hitachi U-3900H UV-Vis spectrophotometer. The sheet resistances of the films were then determined using the four-point probe technique, and then converted into electrical resistivity.

2.2.3 Surface Characterization

Figure 2.10 shows the 2D and 3D AFM images of 100 nm WO_3 films deposited on glass. The films were found very smooth as the rms surface roughness was estimated to be 0.75 nm. Therefore, of the evaporated WO_3 thin films are suitable for developing hybrid inorganic-organic devices as they provide a smooth template for organic thin film deposition.

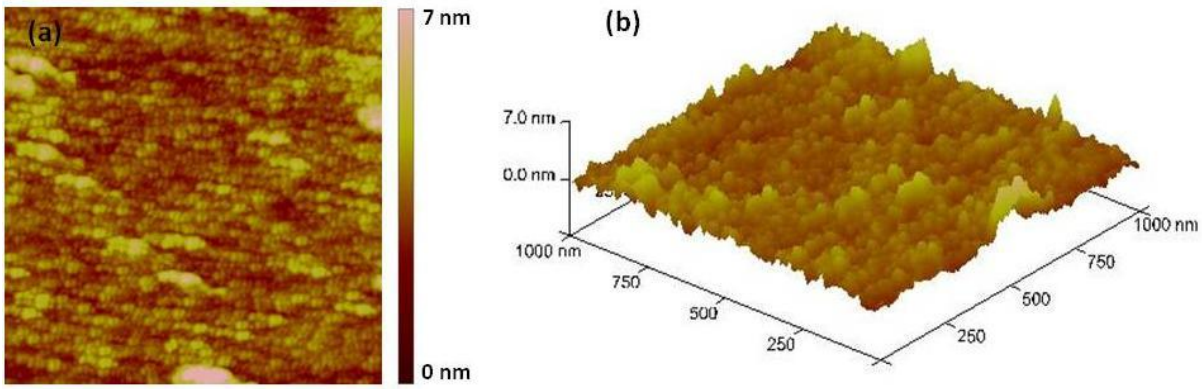

Figure 2.10 AFM images (a) 2D and (b) 3D images of 100 nm WO_3 deposited on glass

2.2.4 Optical Characterization

Figure 2.11 shows the transmission spectra of as-deposited and annealed samples of WO_3 and absorption coefficient spectra of as-deposited film. As seen from the spectra, the WO_3 films have transparency >80% at visible wavelengths. All the post treated samples showed almost identical values of transmission. As-deposited films were slightly less transparent in the region above 650 nm. The results indicate that the evaporation-deposited WO_3 thin films can be used as a transparent electrode in optical devices operating at visible wavelengths.

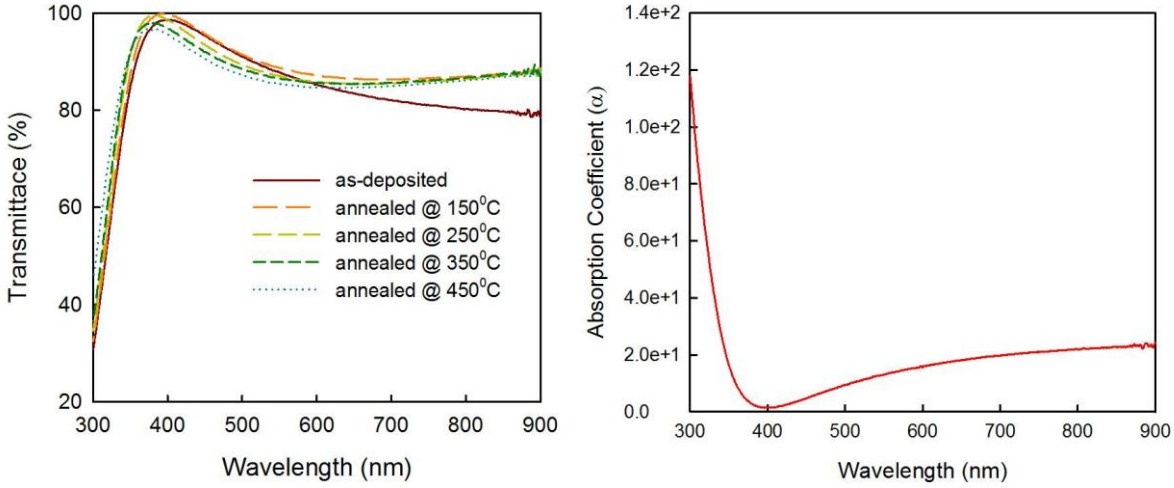

Figure 2.11 Transmission spectra of 100 nm as-deposited and annealed WO_3 films and absorption coefficient of as-deposited film

2.2.5 Electrical characterization

The electrical resistivity of the films annealed at different temperatures is shown in figure 2.12. The resistivity tends to increase slightly after annealing and peaks at 3.6×10^3 Ωcm after 450 ^oC and decreases upon further annealing.

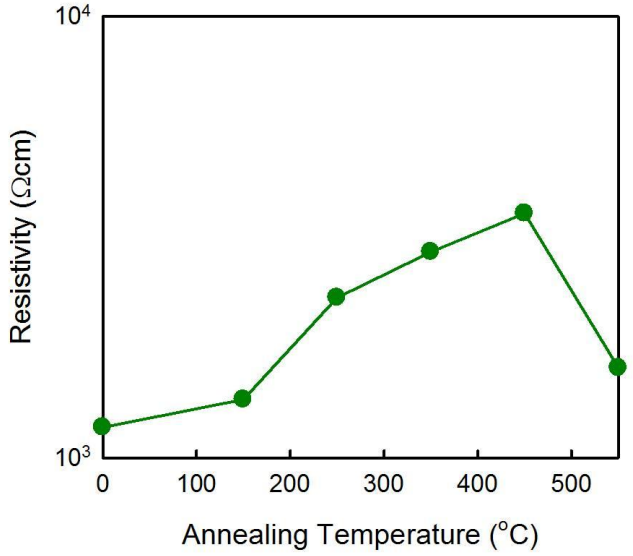

Figure 2.12 Resistivity Vs annealing temperature of a 100 nm WO_3 film on glass

This is due to incorporation of oxygen into the film matrix and crystallization of WO_3 during annealing in air [33]. The relatively small change in the resistivity is consistent with the behavior of the transmission spectrum, which remained similar upon annealing. The results suggest that even though evaporation-deposited WO_3 is not very conductive, it has a higher conductivity than typical organic charge-transporting materials, and can thus be used to act as hole injection and transport layers in hybrid LEDs. .

2.3 Conclusions

In conclusion, we prepared the amorphous thin films of ZTO using thermal co-evaporation with various Zn and Sn compositions. The as-prepared thin films were conductive but not very transparent. However, after post thermal treatment, the films became more transparent. After post annealing at 550 ^{0}C, more than 80% transmission in the visible range was

obtained for ZTO with low Sn atomic contents. These results show that highly conductive and transparent ZTO films can be prepared by thermal co-evaporation followed by thermal annealing. Furthermore, WO_3 thin films were prepared by thermal evaporation. The as-deposited films exhibited a smooth morphology with a roughness of 0.75 nm, high transparency (~90%) in the visible region, and a resistivity ~10^3 Ωcm. Post-deposition annealing had a limited influence on their optical and electrical properties. These investigations suggest that transparent metal oxide thin films may be prepared by thermal evaporation and incorporated into OLEDs to realize facile charge injection and transport.

References

[1] D. S. Ginley and C. Bright, MRS Bull. 25 (2000) 15.

[2] J. H. Yu and G. M. Choi, Sensors and Actuators B: Chem. 72 (2001) 141.

[3] K. L. Chopra, P. D. Paulson, and V. Dutta, Prog. Photovolt. Res. Appl. 12 (2004) 69.

[4] P. Görrn, M. Sander, J. Meyer, M. Kröger, E. Becker, H. H. Johannes, W. Kowalsky, and T. Riedl, Adv. Mater. 18 (2006). 738.

[5] V. Wood, M. J. Panzer, J. E. Halpert, J. M. Caruge, M. G. Bawendi, and V. Bulovic, ACS Nano 3 (2009) 3581.

[6] H. Guo, H. B. Andagana, and X. A. Cao, J. Electron. Mater. 39 (2010) 494.

[7] X. A. Cao, Z. Y. Jiang, and Y. Q, Zhang, Org. Electron. 12 (2011) 306.

[8] T. Minami, H. Sonohara, S. Takata, and H. Sato, Jap. J. Appl. Phys. 33 (1994) L1693.

[9] D. L. Young, H. Moutinho, Y. Yan, and T. J. Coutts, J. Appl. Phys. 92 (2002) 310.

[10] T. Moriga, Y. Hayashi, K. Kondo, Y. Nishimura, K. Murai, and I. Nakabayashi, J. Vac. Sci. Technol. A 22 (2004) 1705.

[11] J. H. Ko, I. H. Kim, D. Kim, K. S. Lee, T. S. Lee, B. Cheong, and W. M. Kim, Appl. Surf. Sci. 253 (2007) 7398.

[12] M. K. Jayaraj, K. J. Saji, K. Nomura, T. Kamiya, and H. Hosono, J. Vac. Sci. Technol. B 26 (2008) 495.

[13] E. Çetinörgü, S. Goldsmith, and R. L. Boxman, Thin Solid Films 515 (2006) 880.

[14] V. K. Jain, P. Kumar, M. Kumar, P. Jain, D. Bhandarid, and Y. K. Vijay, J. Alloys Compounds 509 (2011) 3541.

[15] D. W. Lane, J. A. Coath, K. D. Rogers, B. J. Hunnikin, H. S. Beldon, Thin Solid Films 221 (1992) 262.

[16] M. Asghar, H. Noor, M. Awan, S. Naseem, M. Hasan, Mater. Sci. in Semicond. Proc. 11 (2008) 30.

[17] M. Imada, A. Fujimori, Y. Tokura, Rev. Mod. Phys. 70 (1998) 1039.

[18] M.B. Salamon, Rev. Mod. Phys. 73 (2001) 583.

[19] J. Li, M. Yahiro, K. Ishida, H. Yamada, K. Matsushige, Synth. Met. 151 (2005) 141.

[20] T.Y. Chu, J.-F. Chen, S.-Y. Chen, C.-J. Chen, C.H. Chen, Appl. Phys. Lett. 89 (2006) 053503.

[21] X.Y. Jiang, Z.L. Zhang, J. Cao, M.A. Khan, K.-U. Haq, W.-Q. Zhu, J. Phys. D Appl.Phys. 40 (2007) 5553.

[22] C.C. Chang, J.F. Chen, S.W. Hwang, C.H. Chen, Appl. Phys. Lett. 87 (2005) 253501.

[23] F. Guo, D. Ma, Appl. Phys. Lett. 87 (2005) 173510.

[24] C.W. Chen, Y.-J. Lu, C.-C. Wu, E.H.-E. Wu, Y. Yang, Appl. Phys. Lett. 87 (2005) 241121.

[25] J. Meyer, T. Winkler, S. Hamwi, S. Schmale, H.-H. Johannes, T. Weimann, P. Hinze, W. Kowalsky, T. Riedl, Adv. Mater. 20 (2008) 3839.

[26] J. Meyer, S. Hamwi, T. Bülow, H.-H. Johannes, T. Riedl, W. Kowalsky, Appl. Phys.Lett. 91 (2007) 113506.

[27] S. Tokito, K. Noda, Y. Taga, J. Phys. D Appl. Phys. 29 (1996) 2750.

[28] Appl. Phys. Lett. 91, 113506, (2007).

[29] Appl. Phys. Lett. 96, 193501 (2010).

[30] Appl. Phys. Lett., 94, 4, (2009).

[31] Photovoltaic Specialists Conference (PVSC), 35th IEEE, 1496 – 1499, (2010).

[32] M. Vasilopoulou et al. Thin Solid Films 519 (2011) 5748–5753.

Chapter 3

Development of high efficiency hybrid inorganic-organic light emitting diode (HyLEDs)

3.1 Demonstration of HyLEDs with metal oxide charge transport layers

3.1.1 Introduction

Over the last two decades organic light-emitting diodes (OLEDs) have been the topic of intense research due to their promising applications in flat panel displays. With the successful demonstration of efficient white OLEDs, its interest towards application in solid-state lighting has been started [1]. However, OLEDs are still far from meeting the desired efficiency and operational lifetime for general illumination [2]. State-of-the-art short-wavelength phosphorescent OLEDs suffer significantly from unbalanced charge injection due to poor injection of holes [3-11]. This is because the commonly-used hole-injecting electrode, indium tin oxide (ITO), has a work function ~4.7 eV, which is much lower than the highest occupied molecular orbital (HOMO) of typical hole transport layer (HTL). Therefore, large voltage at the ITO/HTL interface is needed to overcome the energy barrier during device operation, generating equivalent joule's heat. As a consequence, organic materials tend to crystallize and the whole device degradation occurs [4]. Considerable efforts have been made to modify the ITO/HTL interface for enhancing hole injection, such as inserting a thin organic interlayer, which has a HOMO between the Fermi level of ITO and HOMO of the HTL. This acts as a hole injection layer (HIL) [6, 7]

Incorporation of robust inorganic materials into OLEDs as charge injection and transport layers would be an interesting approach to improving the performance of OLEDs, particularly their reliability. Previously, various metal oxide films have been employed as hole injection

layers (HILs) and electron injection layers (EILs) [12-29] in OLEDs. For example, V_2O_5, MoO_3 [30], and WO_3 [31, 32] have been used as a hole injection layer, whereas ZnO and TiO_2 have been used as an electron injection layer. These materials are easy to deposit, and have the benefits of mechanical robustness, low cost, visible light transparency, and good stability. More importantly, they have favorable energy band levels which can effectively reduce the injection barriers for electrons or holes. In many cases, the inorganic HIL creates band bending and effectively displaces the Fermi level of ITO downward thus hole injection is enhanced. A better balance with electron injection leads to improve device efficiency and stability.

It would be highly desirable to develop OLEDs based on a true hybrid inorganic-organic structure, where the inorganic materials play even more important roles, including charge transport. If charge can be injected and transported through inorganic layers into the organic emission region, many vulnerable organic interfaces are eliminated, leading to more efficient and reliable operation of the devices. Up to date, little work has been done to demonstrate such a hybrid inorganic –organic LED (HyLED).

The goal of this work is to demonstrate green phosphorescent HyLEDs with metal oxide charge transport layers, i.e. WO_3 as a HTL and ZTO as an ETL. ZTO and WO_3 thin films developed in Chap. 2 are good candidates as electron and hole transporting materials, respectively, due to their high transparency and good electrical conductivity. As seen in Chap. 2, they can be easily deposited using thermal evaporation in the same system along with organic materials, so the whole HyLED structure may be fabricated in a single run without breaking the vacuum.

3.1.2 HyLEDs with ZTO ETL

Green HyLEDs were fabricated on glass substrates with pre-patterned ITO (sheet resistance ~15 Ω/□). The ITO/glass substrates were cleaned by solvents and deionized water, and exposed to O_2 plasma for 5 min. The samples were then transferred to a thermal evaporation system for the deposition of WO_3 (using WO_3 pellets as the source), 33 at. % Sn ZTO (using co-evaporation) and organic materials. The device structure consisted of a 35 nm WO_3, a 20 nm undoped CBP layer, a 30 nm 4,4'-N,N'-dicarbazolebiphenyl (CBP) doped with 7 wt.% fac-tris(2-phenylpyridinato-N,C2') iridium (III) [$Ir(ppy)_3$] as the emitting layer (EML), and a 15 nm 33 at.% Sn ZTO as an electron transport layer (ETL). Finally, 120 nm Al cathode was deposited through a shadow mask, which defined the active area of the HyLEDs to be ~0.1 cm^2.

The energy band diagram of the fabricated HyLED is shown in Figure 3.1. Simliar device with ZTO replaced by ZnO were also fabricated in separate experiment runs.

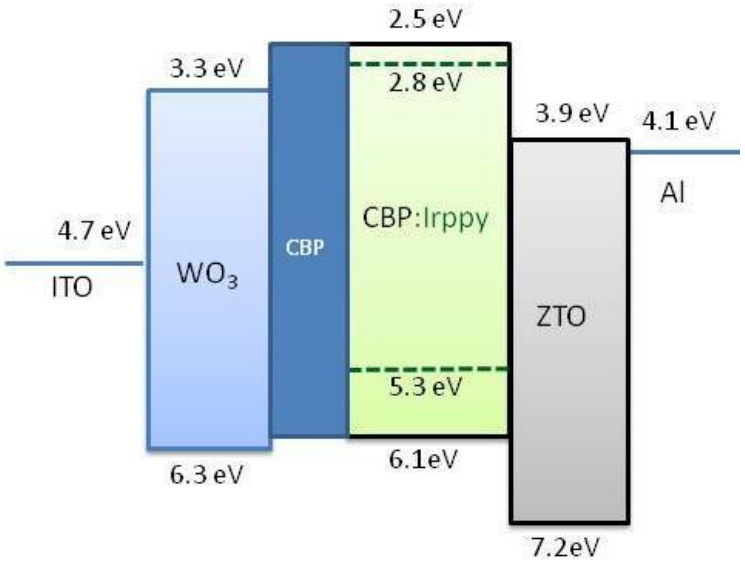

Figure 3.1 Energy Band diagram of HyLED containing ZTO ETL and WO_3 HTL

Under current injection, no light was observed from HyLEDs with both ZTO and WO_3. The forward and reverse IV characteristics as shown in figure 3.2 confirm that the devices are short-circuited. By comparing devices with either WO_3 or ZTO, we concluded that the junction shorting was caused by the ZTO layer. We tried many runs of experiments by varying the parameters such as thickness, deposition rate and composition of ZTO layer, but the results were smilar.

This problem could be attributed to one or all of the following reasons. (i) A relatively large O2 partial pressure exists in the vacuum chamber during the thermal evaporation of ZnO and SnO_2. As a result, a large number of oxygen atoms may be incorporated into the device structure, causing fast degradation of organic materials. (ii) Due to weak metal-O bonds in the amorphous ZTO, oxygen may out-diffuse into the adjacent organic layers under current injection. (iii), the ZTO films are very rough and may contain large defects like pinholes. Al can migrate along the pin holes and make contact to the underlying WO_3 layer, causing junction shorts. .

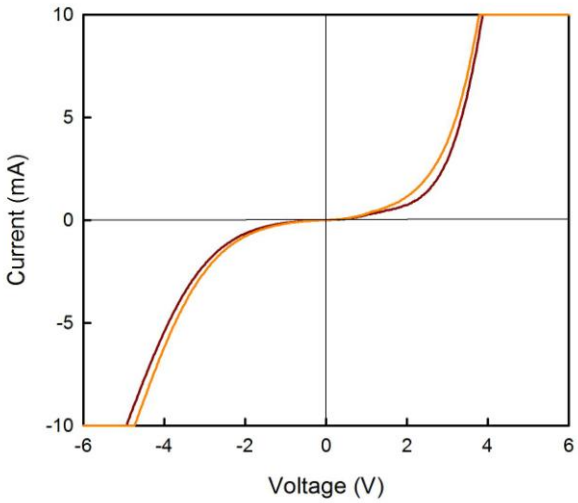

Figure 3.2 IV characteristics of HyLEDs with ZTO as ETL and WO_3 as HTL

Due to the problems associated with ZTO, in the work described below, we will adopt 1, 3, 5-tris(2-N-phenylbenzimidazolyl) benzene (TPBi) as the electron transporting material, and develop HyLEDs with a WO_3 HTL.

3.1.3 HyLEDs with WO_3 HTL

The standard device structure (HyLED A) consisted of a 35 nm WO_3, a 30 nm 4,4'-N,N'-dicarbazolebiphenyl (CBP) doped with 7 wt.% fac-tris(2-phenylpyridinato-N,C2') iridium (III) [$Ir(ppy)_3$] as the emitting layer (EML), and a 45 nm 1,3,5-tris(2-N-phenylbenzimidazolyl) benzene (TPBi) electron transport layer (ETL). Finally, a 0.5 nm LiF/120 nm Al cathode was deposited through a shadow mask, which defined the active area of the HyLEDs to be ~0.1 cm^2. In a modified structure (HyLED B), a 20 nm undoped CBP layer was inserted between the WO_3 and EML as an additional exciton generation zone. For comparisons, OLEDs consisting of a 35 nm N,N-bis-(1-naphthyl)-N,N'-diphenyl-1,1'-biphenyl-4,4'-diamine (NPB) HTL, an optional 20 nm undoped CBP, a 30 nm CBP:7 wt.% $Ir(ppy)_3$ EML and a 45 nm TPBi ETL were also fabricated in the same processing run. The OLEDs without and with an undoped CBP layer are denoted as OLED A and OLED B, respectively. Figure 3.3 shows the band-diagram of fabricated HyLEDs and OLEDs.

The HyLEDs and OLEDs were encapsulated with glass lids in a N_2-filled glovebox and characterized at room temperature. To evaluate the device reliability, as-fabricated devices were stressed at a constant current density of 20 mA/cm^2 in air, and their luminance and voltages were recorded every 10 seconds.

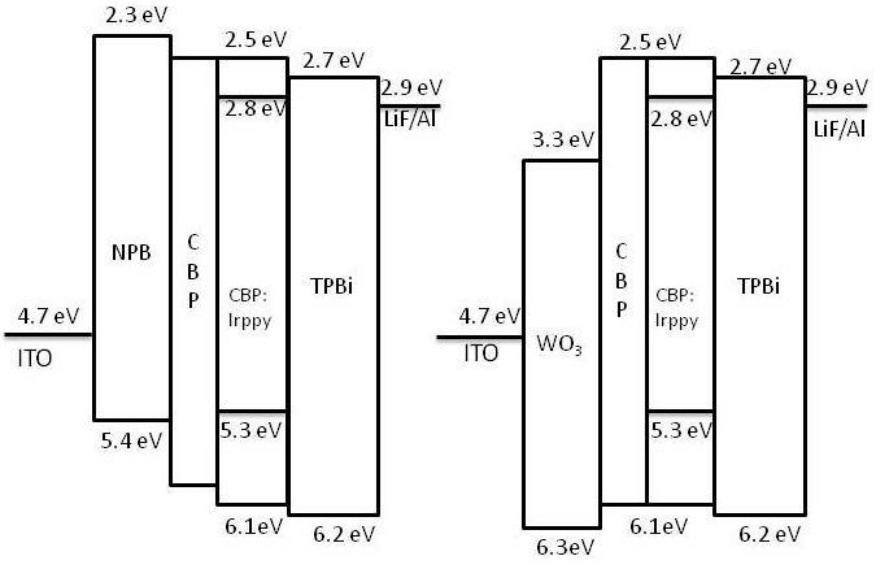

Figure 3.3 Band-diagram of HyLED with WO_3 HTL and an OLED

(a) Current-voltage (IV) comparison

Figure 3.4 compares the current-voltage (I-V) characteristics of the four devices. At 20 mA/cm^2, HyLED A has an operation voltage of 6.1 V, which is 0.8 V lower than that of OLED A.

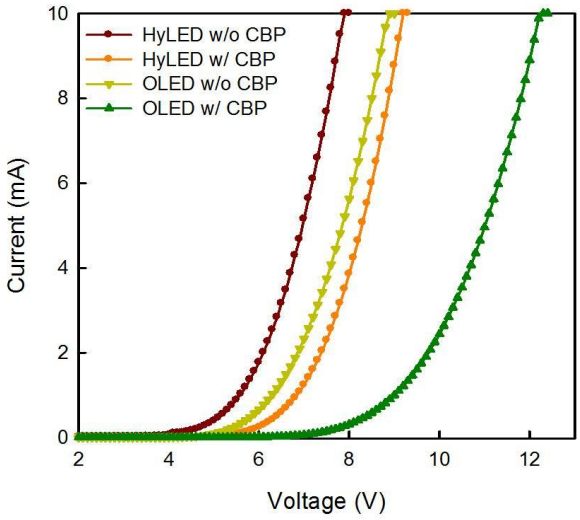

Figure 3.4 IV characteristics of HyLED and OLED with and without undoped CBP

This result confirms more facile hole injection in the HyLED through the WO_3 layer. Adding a 20 nm undoped CBP layer results in an increase in the voltage by 1.3 V in the HyLED (HyLED B) and 2.9 V in the OLED (OLED B). In HyLED B, the undoped CBP does not cause any change in the energy barrier between the WO_3 and EML, as seen from Fig. 3.3. Therefore, the additional 1.3 V voltage is the bias required to maintain charge transport in the undoped CBP.

Meanwhile, the undoped CBP leads to a much larger increase in the voltage in OLED B, which can be explained as follows. As seen in Fig. 3.3, NPB and $Ir(ppy)_3$ have similar HOMO levels, so holes may be injected directly from NPB onto $Ir(ppy)_3$ molecules. The 20 nm undoped CBP blocks this injection path, so all injected holes must overcome the ~0.7 V energy barrier at the NPB/CBP interface to reach the EML.

(b) Luminance - Current (LI) and EQE comparison

The luminance-current (L-I) characteristics of these HyLEDs and OLEDs are compared in Fig. 3.5 (a). At a given current, OLED A is slightly brighter than HyLED A. The former may benefit more from the direct injection of electrons and holes onto $Ir(ppy)_3$ due to more favorable energy level alignments (Fig. 3.3). However, adding a 20 nm undoped CBP has opposite effects on their performance. For the HyLED, the luminance is substantially enhanced. At 20 mA/cm^2, the brightness is increased by 84%, from 5768 cd/m^2 in HyLED A to 10593 cd/m^2 in HyLED B. The external quantum efficiency of HyLED B reaches 13% as shown in Fig. 3.5(b).

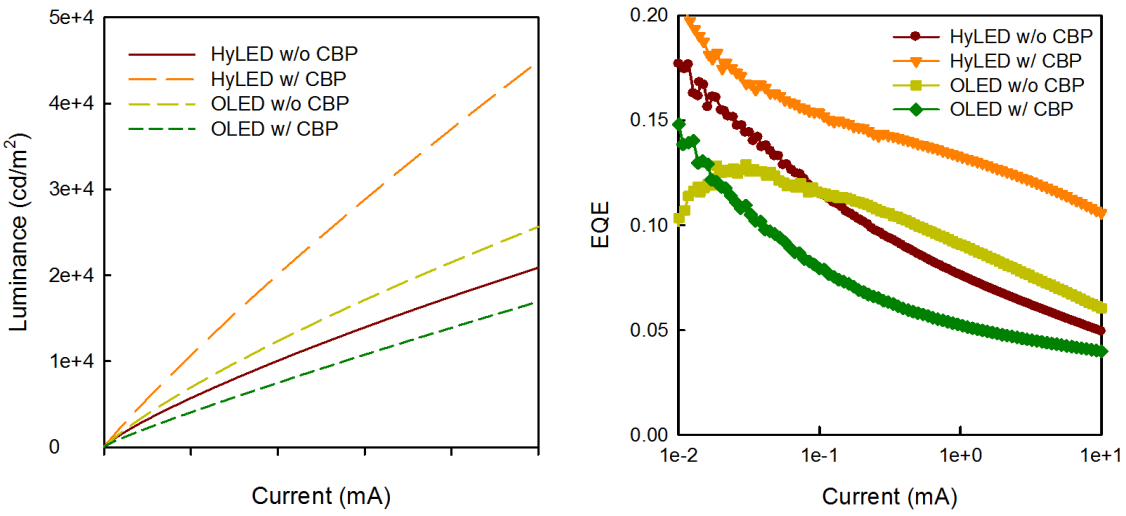

Figure 3.5 (a) Luminance and (b) EQE plots of HyLEDs and OLEDs

In contrast, the luminance of the OLED is decreased by 43%, from 7019 cd/m^2 in OLED A to 4016 cd/m^2 in OLED B. These different behaviors can also be explained based on the energy diagrams in Fig. 3.3. In HyLED B, the undoped CBP captures over-injected electrons and thus broadens the exciton generation zone. Excitons generated in the undoped CBP layer can diffuse or transfer energy to the EML, contributing to the light emission. However, in OLED B, such an effect is overshadowed by the influence of blocked direct injection of holes onto Ir(ppy)$_3$, leading to a decreased luminous efficiency.

(c) Luminance – Voltage (LV) comparison

Figure 3.6 shows the luminance-voltage (L-V) characteristics of all four devices. A brightness of 10^4 cd/m^2 is reached at 6.8 V, 7.3 V, 7.2 V, and 11.3 V for HyLED A, HyLED B,

OLED A, and OLED B, respectively. At this brightness level, HyLED B has current efficiency of 55.2 cd/A, which is 137% higher than that of HyLED A.

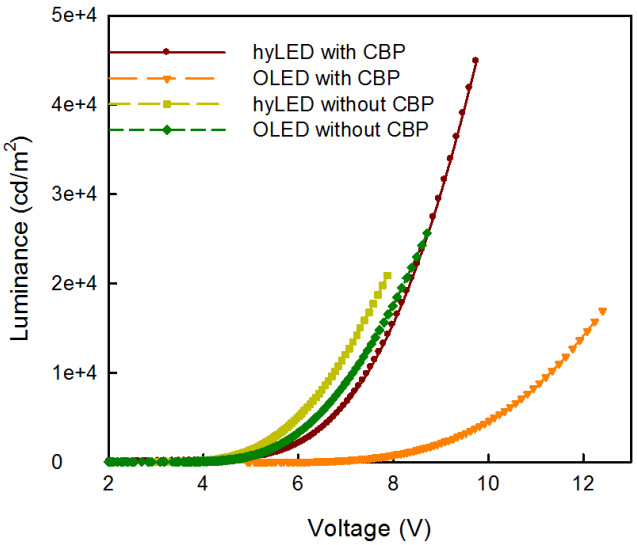

Figure 3.6 Luminance voltage characteristics of HyLEDs and OLEDs

These results show that, even though adding an undoped CBP layer in the HyLED structure results in a small increase in the operation voltage, it greatly improves both the brightness and current efficiency. HyLED B also significantly outperforms the OLEDs. Its current efficiency (cd/A) and power efficiency (lm/W) at 10^4 cd/m^2 are 57% and 55% higher than those of OLED A, respectively.

(d) Lifetime (Reliability) comparison

To evaluate the device reliability, the two brightest emitters, HyLED B and OLED A, were stressed in air at a constant current density of 20 mA/cm^2. The dependence of their normalized luminance and operation voltage on the stressing time is plotted in Fig. 3.7. The OLED exhibits a fast drop in the light intensity, which is accompanied by a rapid increase in the operation voltage.

After 16 h stressing, the luminance decreases by 67%, and the voltage increases by ~2.5V. The HyLED displays much slower degradation. Stressing for 16 h resulted in a decrease in luminance by 22% and a voltage increase by 0.9 V.

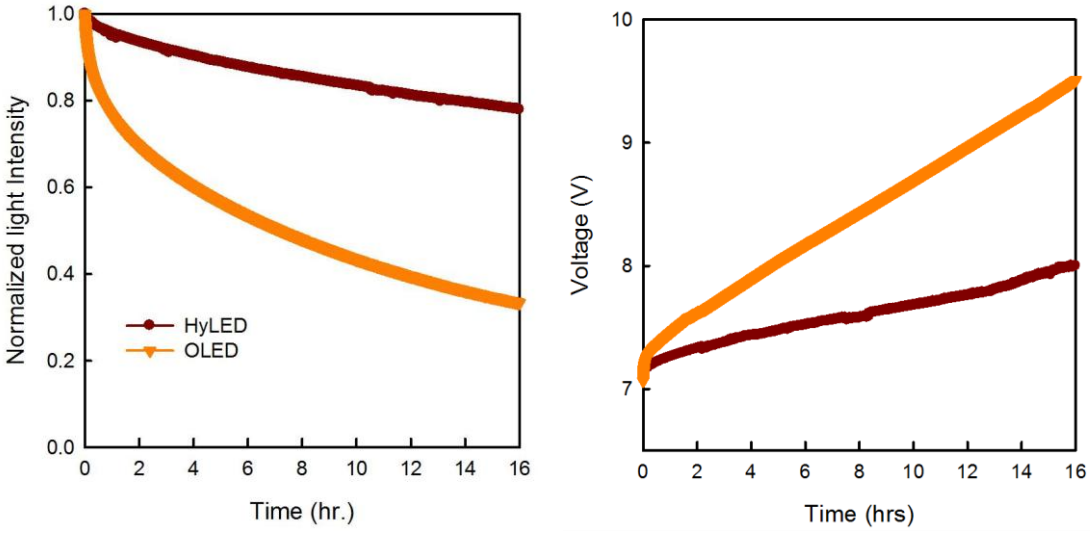

Figure 3.7 Current and voltage reliability plots of HyLED and OLED

The half life (defined as the time for the brightness to decline to 50% of its initial value) of the HyLED is projected to be 52.3 h under this condition, compared to 7.2 h for the OLED. These results demonstrate that the reliability of OLEDs can be greatly improved by using a robust inorganic HTL. In the OLED, a voltage drop at the ITO/NBP interface would produce a large amount of joule heat, accelerating defect generation in amorphous organic materials and interfacial reactions [33]. In the HyLED, WO_3 functions as the HIL and HTL. It reduces the voltage drop and thus heat generation at the interface. More importantly, it has better thermal stability than organic materials and can sustain a higher junction temperature during operation.

3.2 Performance enhancement by structure optimization

3.2.1 Introduction

In the last section, we demonstrated that high-brightness HyLEDs can be realized with a simplified WO_3/organic layer hybrid structure, where WO_3 has a dual function, i.e., hole injection and hole transport. Compared to OLEDs with a NPB HTL, the HyLEDs with a WO_3 HTL had a 57% higher current efficiency at 20 mA/cm^2 and a 7 times longer lifetime under 20 mA/cm^2 stressing. In this section, we conduct a series of experiments to optimize the design of such a green HyLED in order to achieve the best device performance. The layer structure of the device is shown in Fig. 3.8(a). Since electron injection from the LiF/Al electrode is not much an issue, the current study focuses on the optimization of the critical components on the anode side, including (i) the ITO/WO_3 interface; (ii) the WO_3 layer; and (iii) The WO_3/emitting layer (EML) interface, in order to develop HyLEDs with a low operation voltage, a high luminous efficiency, and good operational durability

3.2.2 Device Fabrication

Green phosphorescent HyLEDs with various layer structures as shown in figure 3.8 were fabricated on glass substrates with pre-patterned ITO (sheet resistance ~15 Ω/□). The substrates were first cleaned with solvents and de-ionized water, and subjected to different surface modifications. They were then transferred to a thermal evaporation system, where WO_3, organic materials, and Al were deposited at a rate ~0.1 nm/s. The standard device structure consisted of a 35 nm WO_3 layer, a 20 nm undoped 4,4'-N,N'-dicarbazolebiphenyl (CBP) layer, a 30 nm CBP doped with 7 wt.% fac-tris(2-phenylpyridinato-N,C2') iridium (III) [$Ir(ppy)_3$] as the EML, and a

45 nm 1,3,5-tris(2-N-phenylbenzimidazolyl) benzene (TPBi) electron transport layer. Finally, a 0.5 nm LiF/120 nm Al cathode was deposited through a shadow mask, which defined the active area of the HyLEDs to be ~0.1 cm^2.

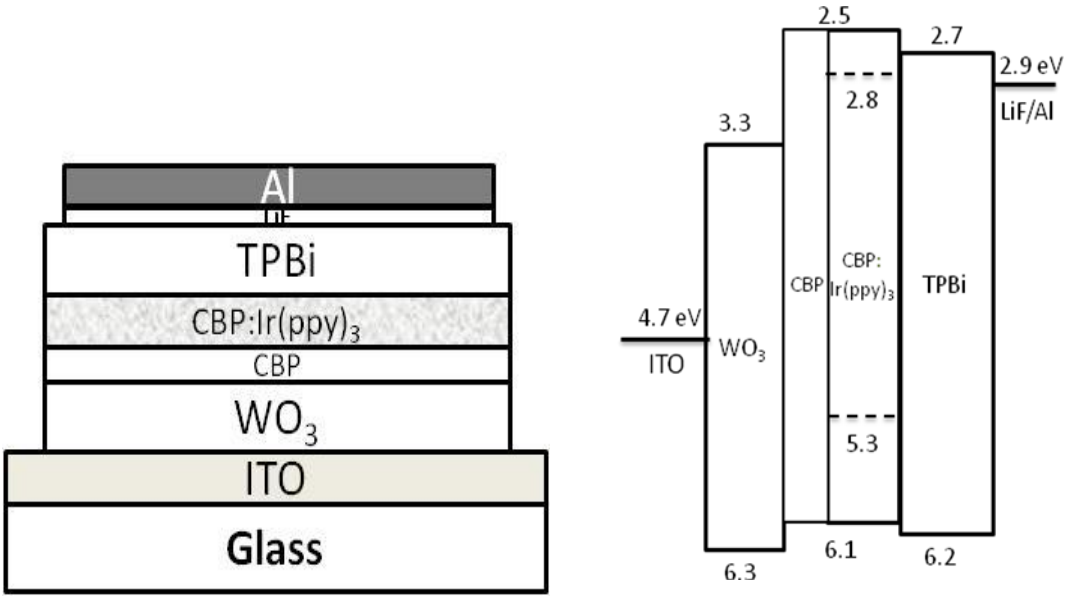

Figure 3.8 Cross section and band diagram of a HyLED

Fabricated HyLEDs were encapsulated with glass lids in a N_2-filled glovebox and immediately their electrical and optical characteristics were measured in air at room temperature. To evaluate the device reliability, as-fabricated devices were stressed at a constant current density of 20 mA/cm^2 in air, and their luminance and voltages were recorded every 10 seconds. In addition, a structure of ITO/WO_3 (100 nm)/ZnO (100 nm)/Al was fabricated for electrical characterization of the ITO/WO_3 interface.

3.2.3 ITO/WO_3 interface optimization

The ITO/WO_3 interface optimization was performed by treating the glass/ITO interface with O_2 and Cl_2 plasma for 5 min. Also, O_2 plasma-treated samples were further coated with 2-10 nm of MoO_x (x~2) by thermal evaporation. The treatment by O_2 and Cl_2 plasma induces a metal-X (x=O, Cl) dipole layer which may significantly raise the work function of ITO [3, 4]. It was found that the MoO_x layer has a work function between those of ITO and WO_3 therefore; it can sustain a voltage drop and effectively elevate the work function of ITO [8, 9].

The current-voltage (I-V) characteristics of standard HyLEDs with ITO treated by different methods can be compared from figure 3.9. As seen, I-V curves of the devices with and without O_2 and Cl_2 plasma treatment are almost identical, showing a turn-on voltage of ~5 V. Even though Cl_2 plasma treatment could raise the work function of ITO by as much as 0.9 eV [4], it caused a minimal reduction in the operation voltage.

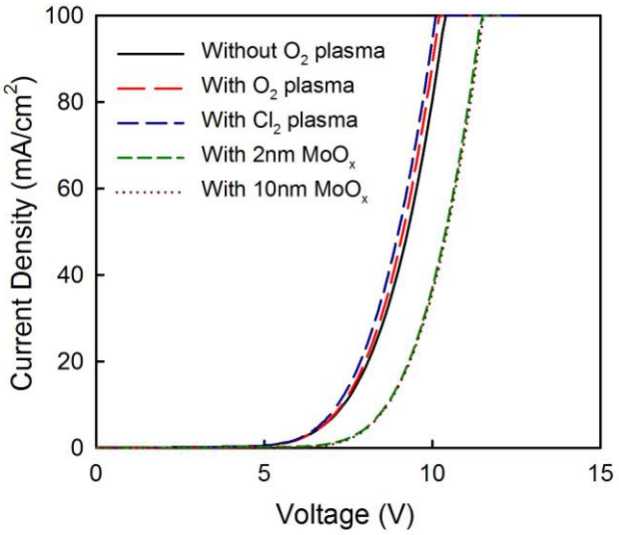

Figure 3.9 Current voltage characteristics of various surface treated standard hyLED

These results indicate that the hole injection is not sensitive to changes of the ITO work function. Also, addition of 2 and10 nm MoO_x resulted in an increase in the forward voltage by ~1 V as seen from the same plot. Typically in OLEDs, it has been found that after the insertion of MoO_x thin layer acting as a HIL sustains a voltage drop needed to reduce the hole injection barrier [8, 9]. However, in the fabricated HyLEDs it seemed that the impact of the interfacial energy barrier is negligible. Instead the extra voltage drop across the MoO_x layer adds to the operation voltage of the HyLEDs.

These results suggest that no additional surface modification of ITO is necessary to enhance hole injection from ITO to WO_3. All the HyLEDs presented hereafter are built on ITO/glass treated with a conventional cleaning procedure, i.e. solvent rinse followed by 5 min O_2 plasma exposure.

We also fabricated a simple ITO/WO_3 (100 nm)/ZnO (100 nm)/Al structure in order to investigate the ITO/ WO_3 interface, where ZnO was also deposited by thermal evaporation and had a low resistivity of 1.8×10^{-4} Ωcm and the I-V characteristic is shown in Fig. 3.10.

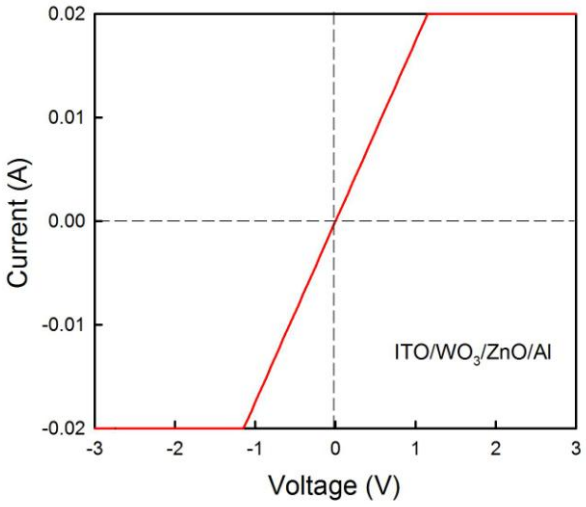

Figure 3.10 Current voltage characteristics of ITO/WO_3/ZnO/Al structure

The linear I-V relationship indicates the ohmic nature of the ITO contact to WO_3. It is plausible that, under a forward bias, holes may tunnel through the interfacial barrier into the valance band or band gap states of WO_3. Therefore, facile injection of holes from the ITO anode into the WO_3 HTL in the HyLEDs is expected. Also seen from the energy diagram in Fig. 3.8, holes can be injected directly from the valance band of WO_3 into the HOMO of CBP.

3.2.4 WO_3 thickness optimization

After understanding the role of tungsten oxide (WO_3) as hole injection and transport layer, next we fabricated devices with various thickness of WO_3 ranging from 5 to 50 nm and compared the performances. Luminance-current-voltage (L-I-V) characteristics of HyLEDs are shown in figure 3.11.

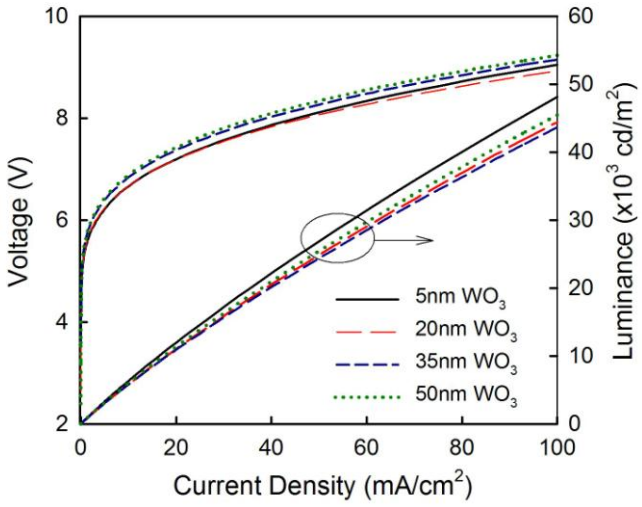

Figure 3.11 L-I-V characteristics of different thickness WO_3 HyLEDs

As seen from the plot, the operation voltages of the devices are very similar at a given current density, indicating that the voltage drop across the different thickness WO_3 layer is quite

small due to its good conductivity and doesn't varies much with thickness. The HyLEDs with 20-50 nm WO_3 showed comparable brightness values, whereas the HyLED with 5 nm WO_3 is slightly brighter (~6%) that reached the luminance level of 10^4 cd/m^2 at ~16.5 mA/cm^2. This is attributed to less light absorption by the thinner WO_3 layer.

Considering the similar turn on voltage and better brightness value, it seems that the thickness of an ideal WO_3 HTL is on the order of a few nanometers. As such a thin layer can act as an effective hole injection and transport layer, while retaining a high transparency for visible light. However, another critical design consideration is the impact of the WO_3 layer on the reliability of the HyLED, because the ITO/HTL interface plays a critical role in device operation [4].

Therefore, in order to evaluate the reliability, all the fabricated HyLEDs were stressed in air at 20 mA/cm^2 current density and the results of the normalized luminance versus stressing time is plotted in the figure 3.12.

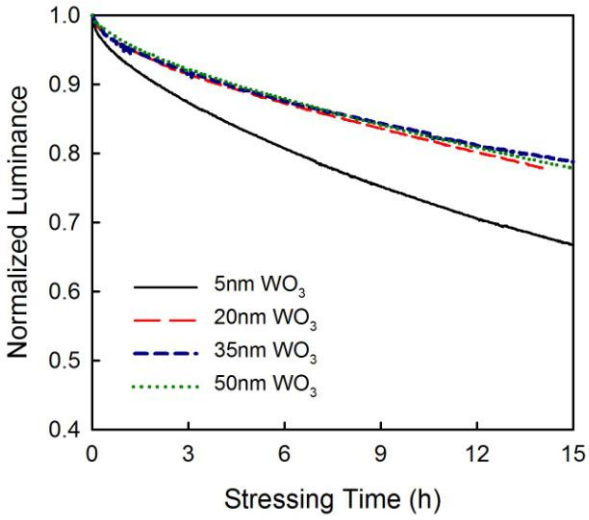

Figure 3.12 Reliability plots for various thicknesses WO_3 based HyLEDs

It was found that the HyLEDs with 20-50 nm WO_3 displayed relative slower and similar degradation rate and better reliability than with 5 nm. For 20-50 nm WO_3 devices stressing for 15 h resulted in a decrease in luminance by ~21%. Similarly, their half life (defined as the time for the brightness to decline to 50% of its initial value) is projected to be ~52 h under this condition. However, the HyLED with 5 nm WO_3 exhibited a considerably faster drop in the light intensity and after 15 h stressing, the luminance decreased by 33%. Also seen from the plot, the faster luminance decay was accompanied by a rapid increase in its operation voltage and the estimated half life was only about 30 h.

It was thus found that HyLEDs with a 20-50 nm WO_3 HTL were much more durable even though they were less bright. However, few nanometer-thick WO_3 layer may not form a uniform and robust film which can effectively prevent the interfacial reactions between ITO and organic materials. Therefore, our study suggested that the relatively thick WO_3 HTL should be adopted to ensure efficient and reliable operation of the HyLED.

3.2.5 WO_3/EML optimization

The next step of optimization was to investigate the WO_3/EML interface. We first fabricated devices with and without undoped CBP layer inserted between WO_3 and EML. Four HyLED structures were compared (i) 0 nm undoped CBP (without CBP layer), (ii) 10 nm undoped CBP, (iii) 20 nm undoped CBP and (iv) 30 nm undoped CBP. Both the HyLEDs with and without an undoped CBP showed the typical green electroluminescence of $Ir(ppy)_3$ with a peak wavelength of 517 nm.

From figure 3.13, L-I-V characteristics of the HyLEDs with 0-30 nm undoped CBP can be compared. At a given current density, the luminance increased as the undoped CBP layer thickness increased, and tends to saturate at 20-30 nm. At 20 mA/cm^2, the brightness of the

HyLED with 0 nm undoped CBP is 6212 cd/m^2. This value is increased to 8578 cd/m^2, 10713 cd/m^2, and 11642 cd/m^2 for HyLEDs with 10 nm, 20 nm, and 30 nm undoped CBP, respectively. The external quantum efficiency and current efficiency of the device with 30 nm undoped CBP were 14.2% and 58.2 cd/A, respectively, and the values are 87.4% higher than those of the HyLED with 0 nm undoped CBP.

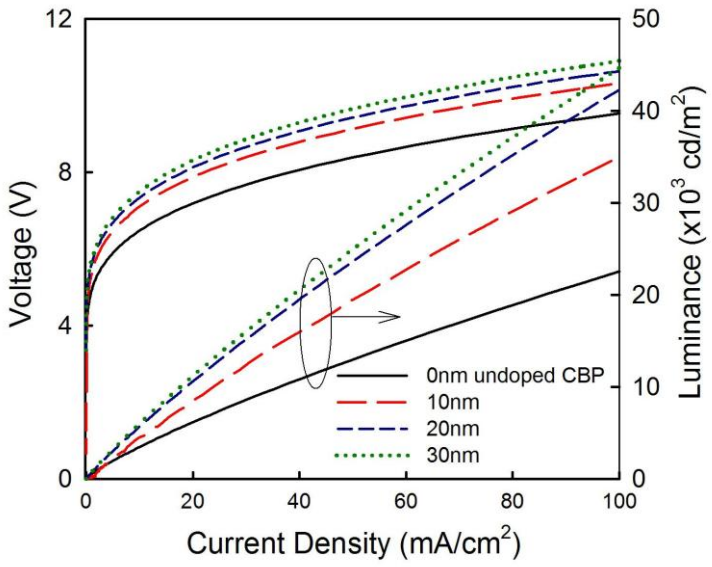

Figure 3.13 L-I-V characteristics of HyLEDs with 0-30 nm undoped CBP layer

The undoped CBP assisted in capturing over-injected electrons and meanwhile acted as a reasonable hole transport layer, leading to a broadened exciton generation zone. Excitons generated in the undoped CBP layer can thus diffuse or transfer energy to the CBP:Ir(ppy)$_3$ (EML), contributing to the additional light emission. Also seen in figure 3.2.7, the operation voltage also increases with the increase in thickness of the undoped layer. It is ~1.1 V higher in the HyLED with 30 nm CBP at 20 mA/cm^2 than with 0 nm CBP. This additional voltage is believed to be required to drive charge transport across the undoped CBP layer.

The above results confirmed that, even though an inserted undoped CBP layer results in a small increase in the operation voltage, it greatly improved the brightness, current efficiency as well as luminous efficiency of the HyLED. The optimal thickness therefore has been determined to be ~30 nm.

Second, we fabricated device with an electron blocking layer 4,4',4''-tris(N-carbazolyl)-triphenylamine (TCTA) inserted in between WO_3 and the EML. 20 nm TCTA was thermally evaporated forming a device structure as shown in the band diagram (figure 3.14). As seen from the band diagram, LUMO level of TCTA is at 2.3 eV which is higher than that of EML, so the blocking of electrons is expected. For, comparison standard device structure with 20 nm undoped CBP was also fabricated in the same run and the performance were studied.

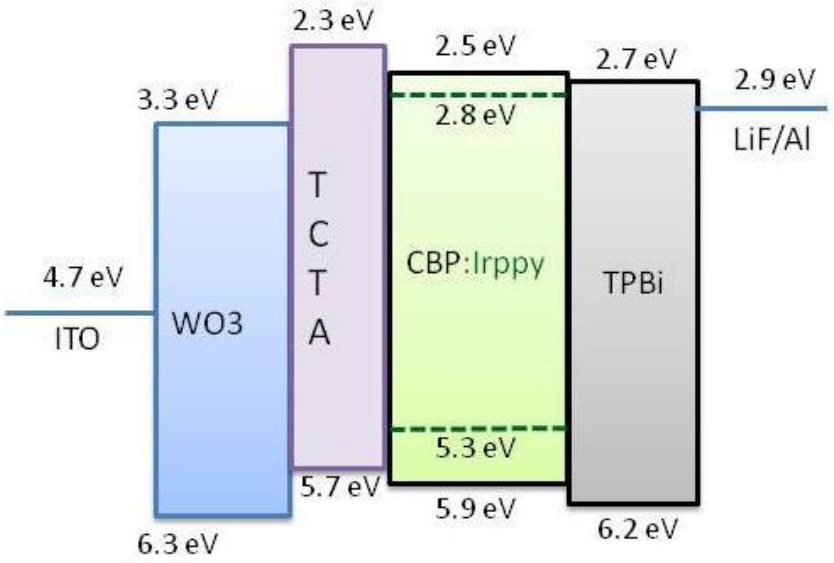

Figure 3.14 Band-diagram of HyLED structure with TCTA e-blocking layer

Figure 3.15 below compares the current-voltage characteristics of the two structures. As seen, turn on voltage in HyLED with TCTA electron blocking layer was approximately 1.8 V

higher than that of without TCTA layer. Similarly, photocurrent versus current plots is shown in figure 3.2.9. HyLED without TCTA were much brighter than with TCTA layer. Although, it seems that the addition of TCTA improves the performance, our results confirmed otherwise. This could be attributed to the inefficient hole injection from WO_3 into the CBP host or the EML layer, as can be seen from the band-diagram.

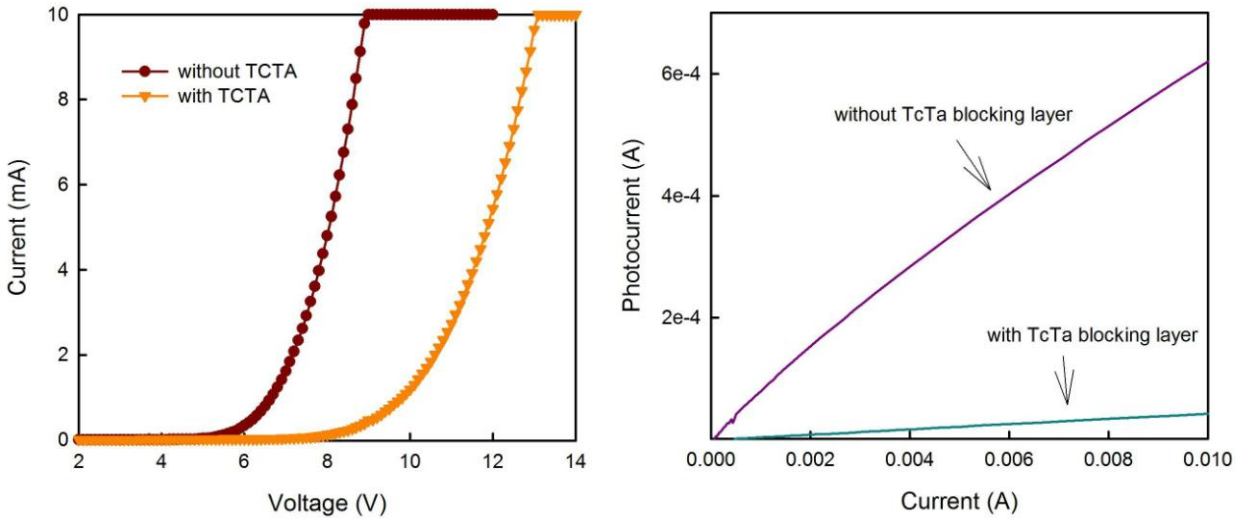

Figure 3.15 IV and LI plots for HyLEDs with and without TCTA layer

3.2.6 EML thickness optimization

We fabricated three HyLED devices having 20 nm, 30 nm and 50 nm thickness of EML – 7 wt. % $Ir(ppy)_3$ doped in a CBP host. The remaining layers are similar to the standard structure having 35 nm WO_3 and 20 nm undoped CBP. As seen from the IV plot (figure 3.16), device with 20 nm EML has the lowest turn on voltage and which increased with the increase in EML thickness. The additional voltage is required to move electrons and holes within the thicker EML. Broadening the thickness of EML, although creates additional exciton formation and recombination zone it uses more potential to move the charge carriers.

Also seen from the figure 3.16, the luminance (photocurrent) value of 30 nm thick EML is highest. It seems that the thicker EML has more exciton formation and recombination zone, but there is an optimum value for the thickness. Therefore, the optimum value of EML thickness chosen was 30 nm.

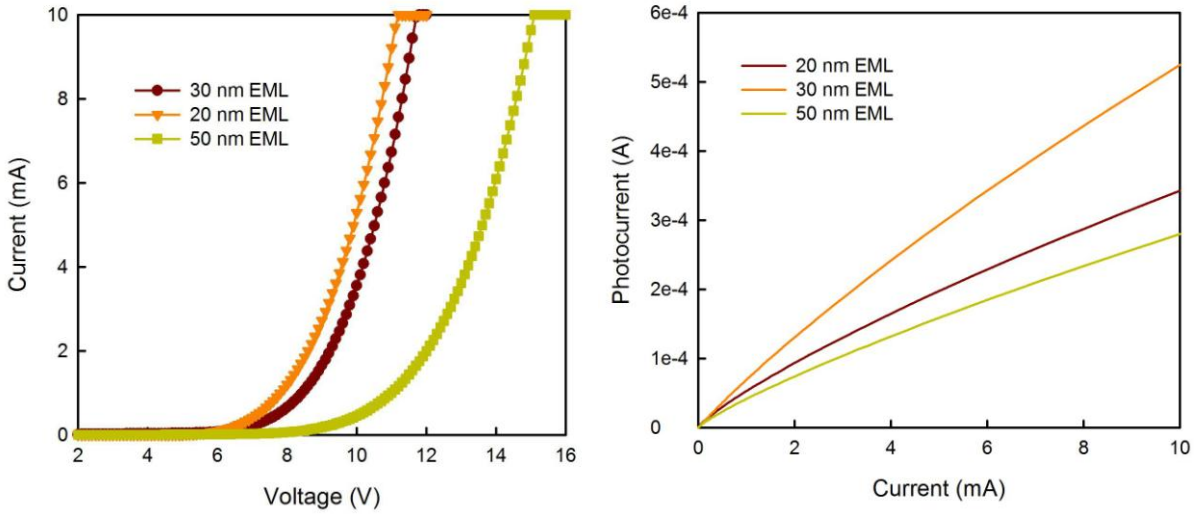

Figure 3.16 IV and LI plots for various thickness of EML in HyLEDs

3.3 Conclusions

In conclusion, we have demonstrated high-brightness green HyLEDs based on a simplified WO_3/organic layer structure. The HyLEDs comprised a WO_3 HIL and HTL, and had a low operation voltage of 6.1 V due to improved balance of charge injection, which was 0.8 V lower than that of OLEDs with an organic NPB HTL. The brightness value of 10^4 cd/m^2 was reached at 7.3 V. At this brightness level, the current efficiency and power efficiency of the HyLED were 57% and 55% higher than those of the OLED, respectively. Also, the hybrid structure markedly improved the device half-life by a factor of 7 due to a more stable ITO/HTL

interface.Through structure optimization, it was concluded that 20-50 nm as-deposited WO_3 layer has critical attributes for hole transport, including high transparency, low resistivity, and good physical stability. Adding a 20-30 nm undoped CBP layer between the WO_3 and CBP:$Ir(ppy)_3$ EML significantly enhanced the HyLED performance. This simplified hybrid structure represents a viable design for efficient and durable OLEDs suitable for display and lighting applications.

References

[1] S. Reineke, F. Lindner, G. Schwartz, N. Seidler, K.Walzer, B. Lu¨ssem, K. Leo, Nature 2009, 459, 234

[2] F. So, J. Kido, and P. Burrows, MRS Bull., 33, 663-669, 2008.

[3] C. C. Wu, C. I. Wu, J. C. Sturm, and A. Kahn, Appl. Phys. Lett., 70, 1350-1352, 1997.

[4] X. A. Cao and Y. Q. Zhang, Appl. Phys. Lett.,100, 183304, 2012.

[5] Y. Q. Zhang, R. Acharya, and X. A. Cao, J. Appl. Phys.,112, 013103, 2012.

[6] K. R. Choudhury, J. Lee, N. Chopra, A. Gupta, X. Jiang, F. Amy, and F. So, Adv. Funct. Mater. 19,491-496, 2009.

[7] S.F. Chen, C. W. Wang, Appl. Phys. Lett.,85, 765-767, 2004.

[8] I. Irfan, H. Ding, Y. Gao, D. Y.Kim, J. Subbiah and F. So, MRS Proc. Vol. 1212, 1212-S08-05, 2009.

[9] T. Matsushima and H. Murataa, Appl. Phys. Lett., 95, 203306, 2009.

[10] J. Li, M. Yahiro, K. Ishida, H. Yamada, and K. Matsushige, Synth. Met., 151,141-146, 2005.

[11] J. Meyer, S. Hamwi, T. Bülow, H. H. Johannes, T. Riedl, and W. Kowalsky, Appl. Phys. Lett.,91,113506, 2007.

[12] H. J. Bolink , E. Coronado , J. Orozco , M. Sessolo , Adv. Mater. 2009, 21, 79.

[13] S. A. Haque , S. Koops , N. Tokmoldin , J. R. Durrant , J. S. Huang , D. D. C. Brandley , E. Palomares , Adv. Mater. 2007, 19, 683.

[14] N. Tokmoldin , N. Griffi ths , D. D. C. Bradley , S. A. Haque , Adv. Mater. 2009, 21, 3475.

[15] H. J. Bolink , E. Coronado , D. Repetto , M. Sessolo , E. M.Barea , J. Bisquert , G. Garcia-Belmonte , J. Prochazka , L. Kavan , Adv. Funct. Mater. 2008, 18, 145.

[16] K. S. Yook , S. O. Jeon , C. W. Joo , J. Y. Lee , Appl. Phys. Lett. 2008, 93, 013301 – 1.

[17] L. C. Palilis, M. Vasilopoulou , D. G. Georgiadou , P. Argitis , Org. Electr. 2010, 11, 887.

[18] J. Meyer, T. Winkler, S. Hamwi , S. Schmale , H.-H. Johannes, T. Weinmann , P. Hinze , W. Kowlasky , T. Riedl , Adv. Mater. 2008, 20, 3839.

[19] J. Meyer, S. Hamwi, T. Bülow , H.-H. Johannes, T. Riedl , W. Kowalsky , Appl. Phys. Lett. 2007, 91, 113506.

[20] J. Meyer, S. Hamwi, S. Schmale, T. Winkler, H.-H Johannes, T. Riedl, W. Kowalsky J. Mater. Chem. 2009, 19, 702.

[21] M. Kroger, S. Hamwi , J. Meyer , T. Riedl ,, W. Kowalsky , A. Kahn , Org. Electr. 2009, 10, 932.

[22] S. Hamwi, J. Meyer, M. Kröger, T. Winkler, M. Witte, T. Riedl, Kahn, W. Kowalsky, Adv. Funct. Mater. 2010, 20, 1.

[23] C. C. Chang, M. T. Hsieh, J. F. Chen, S. W. Hwang, C. H. Chen , Appl. Phys. Lett. 2006, 89, 253504.

[24] M. J. Son, S. Kim, S. Kwon, J. W. Kim, Org. Electr. 2009, 10, 637.

[25] H. M. Zhang, W. C. H. Choy, Org. Electr. 2008, 9, 964.

[26] T. Matsushima, Y. Kinoshita, H. Murata, Appl. Phys. Lett. 2007, 91, 253504.

[27] H. You, Y. Dai, Z. Zhang, D. Ma, J. Appl. Phys. 2007, 101, 026105.

[28] F. Guo, D. Ma, Appl. Phys. Lett. 2005, 87, 173510.

[29] M. Bär, L. Weinhardt, B. Marsen, B. Cole, N. Gaillard, E. Miller, C. Heske, Appl. Phys. Lett. 2010, 96, 032107.

[30] C.W. Chu, S.-H. Li, C.-W. Chen, V. Shrotriya, and Y. Yang, Appl. Phys. Lett. 8, 193508 (2005).

[31] H. Kanno, R. J. Holmes, Y. Sun, S. Kena-Cohen, and S. R. Forrest, Adv. Mater. Weinheim, Ger., 18, 339, (2006).

[32] Y. Han, D. Yanfeng, Z. Zhiqiang, and M. Dongge, J. Appl. Phys. 101, 026105 (2007)

[33] X. A. Cao and Y. Q. Zhang, Appl. Phys. Lett. 100, 183304 (2012).

Chapter 4

Development of inverted structure HyLEDs

4.1 Introduction

To develop large area, high-resolution OLED-based flat panel displays an active matrix driving method is needed [1]. Low-temperature polycrystalline silicon (LTPS) and amorphous silicon (*a*-Si) thin film transistor (TFT) backplane technologies are used in active matrix OLEDs (AMOLEDs) [1]. Smaller handheld portable consumer products, such as mobile display camera and personal digital assistant (PDA) have already utilized LTPS TFT technology as the backplane for their OLED displays. However, LTPS requires complex fabrication process and is limited by the size of the available substrates [1, 2]. Therefore, *a*-Si technology is getting popular for large display applications, such as TVs, due to its low manufacturing cost and high yield. However, it is recognized that a-Si TFTs and conventional OLED architectures are not very compatible. Conventional bottom-emitting OLEDs comprise a device layer structure deposited on a transparent ITO bottom anode. However, only *n*-channel TFT can be used in *a*-Si backplanes, which necessitates the bottom contact of the OLED as the cathode and thus requires OLEDs to have an inverted structure. Therefore, there is a need to develop an inverted structured OLED compatible with the *a*-Si TFT technology. Such an OLED consists of a bottom cathode and a top anode. Bottom cathode can be thus directly connected to the n-type TFT drain line, resulting in a decrease in driving voltage and improved stability [3,4]**.** Light may be emitted from bottom or top, depending on whether the bottom cathode is transparent or reflective. If the bottom cathode is reflective, then light is emitted from the top, and the device is known as an inverted top emission OLED (ITOLED) [5-7]**.** Whereas, if the bottom cathode is transparent and

the anode is reflective, light is emitted from the bottom and the device is known as an inverted bottom emission OLED (IBOLED) [8].

ITOLEDs have been fabricated using reflective metals, such as MgAg [9], Al [10-14] as the bottom cathode and using sputtered ITO as the top anode. However, the performances of the devices were poor because of damage to the organic layers caused by the high energy radiation of the sputtered species [15]. A few papers reported on the use of a protecting layer on top of the organic structure to reduce the radiation induced damage caused by sputtering [9, 16-18]. There are also reports on replacing the top ITO anode with a thin film of Au [19, 20], NiO [21], IZO [22], or Ag/TeO_2 [23]. However, there might be variations in the EL spectra with different viewing angles caused by a microcavity effect due to two (cathode and anode) reflective and/or semi-transparent metal electrodes [24].

The goal of this work is to develop an efficient IBOLED based on a simplified hybrid inorganic-organic structure, which may avoid the above-mentioned problems associated with ITOLEDs. One major challenge in fabricating IBOLEDs on ITO substrates is that the high work function of ITO impedes efficient electron injection. Efforts have been made to improve electron injection from ITO by depositing a thin film of low work function materials including Al, Al/Liq [25], Cs [25], Mg [25], Ag/Liq [25], Mg [25], and Mg/Cs2O:Bphen [1] on top of ITO. In this study, we will evaluate the efficiency of electron injection from a nanometer thick Al or Ca deposited on ITO substrates, and its balance with hole injection from an Al anode into WO_3.

4.2 Device Fabrication

Green phosphorescent inverted bottom emission HyLED having layers as shown in figure 4.1 (a) were fabricated in pattered ITO/glass substrate. The substrates were first cleaned with

solvents and de-ionized water and were then transferred to a thermal evaporation system, where WO_3, organic materials, Ca and Al were deposited. The three devices were fabricated with Al (3nm)/LiF(0.5nm), Ca (3nm), Ca(3nm)/LiF(0.5nm), as different types of electron injection layer deposited on top of ITO cathode. For comparison, fourth device without any injection layer was also fabricated. A 45 nm 1,3,5-tris(2-N-phenylbenzimidazolyl) benzene (TPBi) electron transport layer, a 30 nm CBP doped with 7 wt.% fac-tris(2-phenylpyridinato-N,C2') iridium (III) [$Ir(ppy)_3$] as the EML, a 20 nm undoped 4,4'-N,N'-dicarbazolebiphenyl (CBP) layer and a 35 nm WO_3 HTL were subsequently deposited. Finally, 120 nm Al anode was deposited through a shadow mask, which defined the active area of the inverted HyLEDs to be ~0.1 cm^2. All the device structures were deposited without breaking the vacuum.

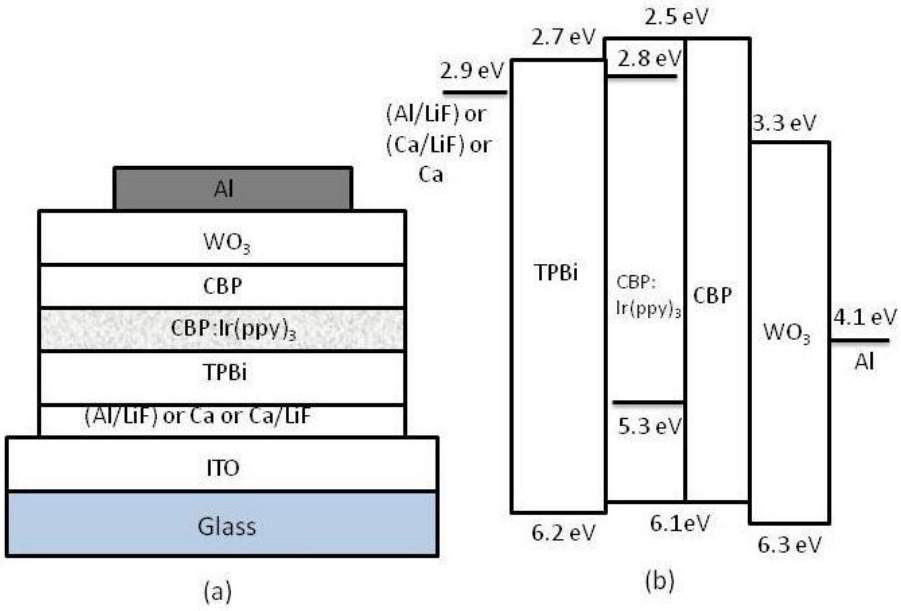

Figure 4.1 Showing (a) cross-section and (b) band diagram of an inverted HyLED

Fabricated inverted HyLEDs were encapsulated with glass lids in a N_2-filled glovebox and immediately their electrical and optical characteristics were measured in air at room temperature

as mentioned in chapter 2. To evaluate the device reliability, as-fabricated devices were stressed at a constant current density of 20 mA/cm^2 in air, and their luminance and voltages were recorded every 10 seconds.

4.3 Results and discussion

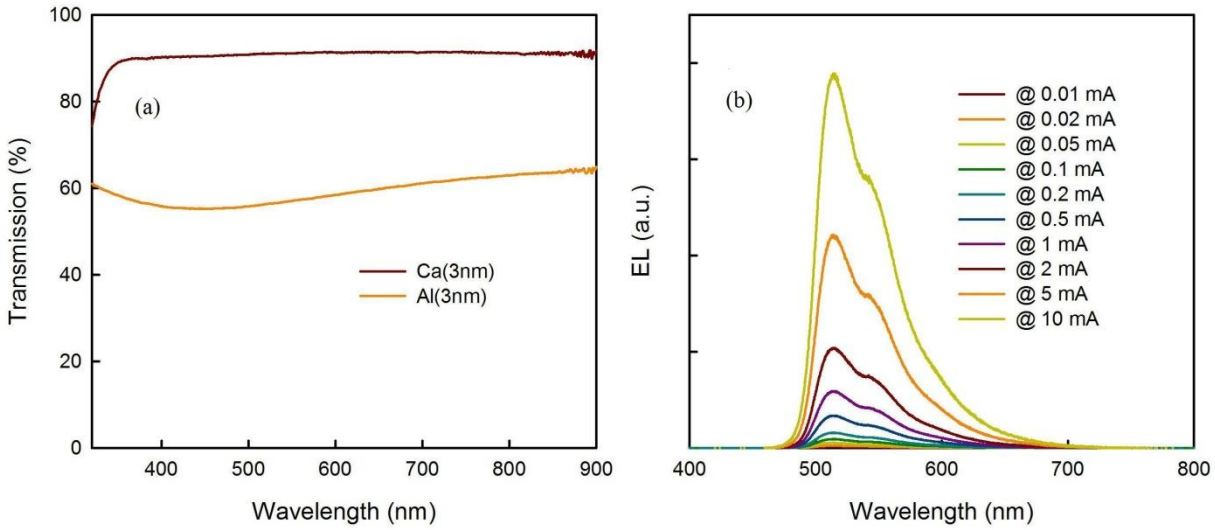

Figure 4.2 (a) Transmission spectra of 3nms Ca and Al film on glass and (b) EL spectra of Ca only inverted HyLED with different currents

All the fabricated inverted HyLEDs, except without electron injection layer showed typical bright green emission of $Ir(ppy)_3$ phosphorescent emitter as seen from the EL spectra in Fig. 4.2 (b). The transmission spectra of 3 nm thin films of Ca and Al deposited on ITO/glass substrates are shown in Fig 4.2 (a). As seen, as-deposited films of Ca are highly transparent in the visible region (~90%) whereas as-deposited Al films are only ~60% transparent.

4.3.1 Current-Voltage (I-V) Characteristics

Figure 4.3 compares the current-voltage characteristics of four devices. As seen from the plot, turn-on voltage of the inverted HyLED is greatly improved from ~15 V to ~ 7 V, with the addition of electron injection layers (Al/LiF, Ca, and Ca/LiF). The device without electron injection layer showed no light emission, but exhibited considerable current, indicating hole dominated device.

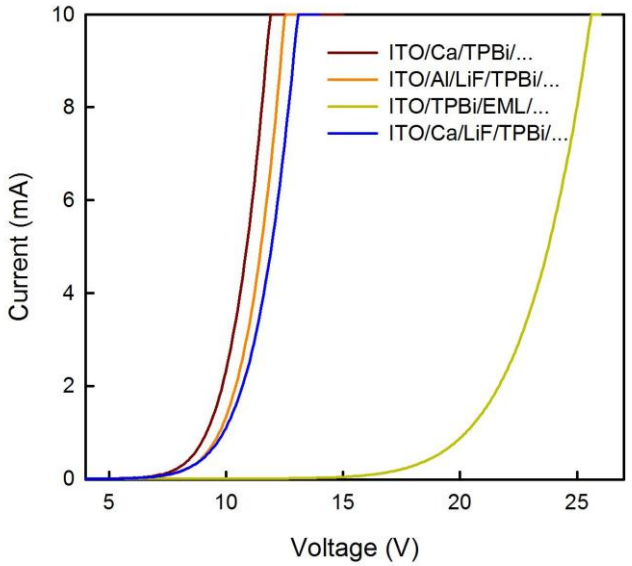

Figure 4.3 Current-voltage characteristics of inverted HyLEDs

Several mechanisms have been proposed to explain the enhanced electron injection originating from lowering of the barrier height between the cathode's Fermi level and the LUMO of the organic material. Among which, chemical reaction model [35, 36] and dipole model [37, 38] are more popular ones. Electron injection is enhanced by the formation of radical ions, such as Alq_3^-, in case of (Alq3-LiF-Al) trilayer [39] injection layer as explained by chemical reaction model. Whereas in a dipole model, the electric potential across the dipole layer reduces the

interfacial barrier for electron injection. It is obvious from the IV plot, that the electron injecting capability is comparable amongst three injection layers where 3 nm Ca only device showing the best performance.

4.3.2 Luminance-Current (L-I) Characteristics

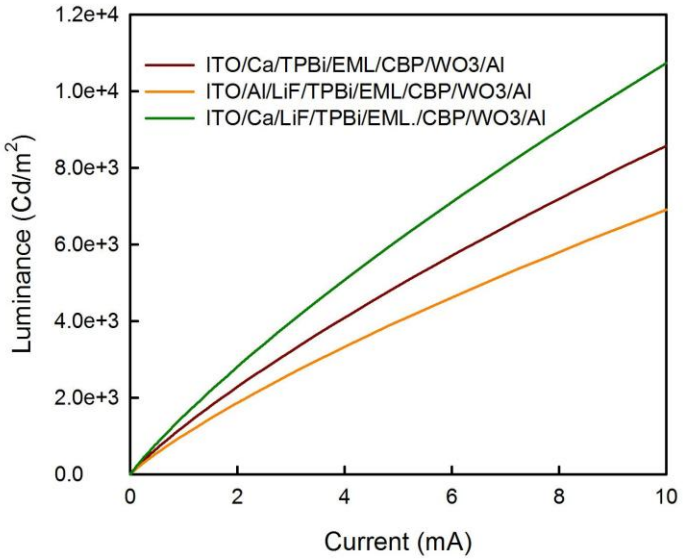

Figure 4.4 Luminance-current characteristics of inverted HyLEDs

Figure 4.4 compares the luminance Vs current values of inverted HyLEDs with various electron injecting layers. The device with Ca/LiF electron injecting layer was the brightest with a luminance of 2780 Cd/m^2 at 20 mA/cm^2, Ca only device showed the luminance of 2260 Cd/m^2 and Al/LiF device showed the luminance of 1850 Cd/m^2 at 20 mA/cm^2.

Since, 3nm Al film is only 60% transparent, the luminance value of device containing Al/LiF is lower. Similarly, 3 nm Ca film being 90% transparent, the luminance value is higher.

The electron injection from the device with Ca/LiF must have balanced the hole injection from WO_3, as a result they are more brighter than the Ca only device.

The EQE of all the three devices are shown in the figure 4.5. The devices with Ca/LiF, Ca and Al/LiF have EQE of 8.8%, 7.8% and 6.2% respectively at current density of 20 mA/cm^2.

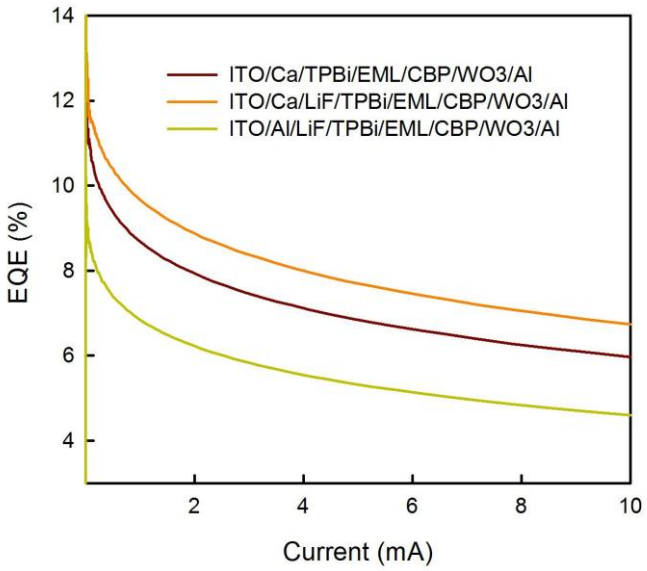

Figure 4.5 External quantum efficiencies (EQEs) of inverted HyLEDs

4.3.3 Luminance-voltage (L-V) characteristics

Luminance values of three devices are plotted against voltage in figure 4.6. At 12.8 V the maximum luminance of 10357 Cd/m^2 is reached for Ca/LiF electron injection. Similarly, at 12 V, maximum luminance value of 6903 Cd/m^2 is reached for Al/LiF and at 11.9 V the maximum luminance of 8579 Cd/m^2 is reached for Ca only device.

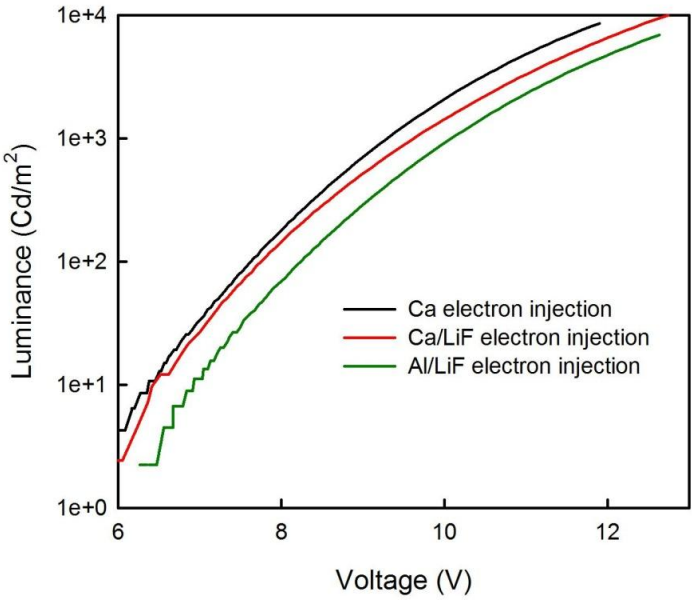

Figure 4.6 Luminance-voltage characteristics of inverted HyLEDs

4.3.4 Device Reliability

The results of the photocurrent (luminance) and voltage reliability of devices upon stressing the devices with constant current density of 20 mA/cm^2 are shown in figure 4.7 (a) and (b). The device with Ca electron injection layer showed better reliability compared to Al/LiF electron injection layered device. The half life-time of former being at 23.4 hours while only 15.7 hours for later.

The result is consistent with the higher rate of voltage increase in the Al/LiF based device as shown in figure 4.7 (b). Therefore, ITO/Ca/TPBi interface is more stable than ITO/Al/LiF/TPBi interface in terms of device reliability.

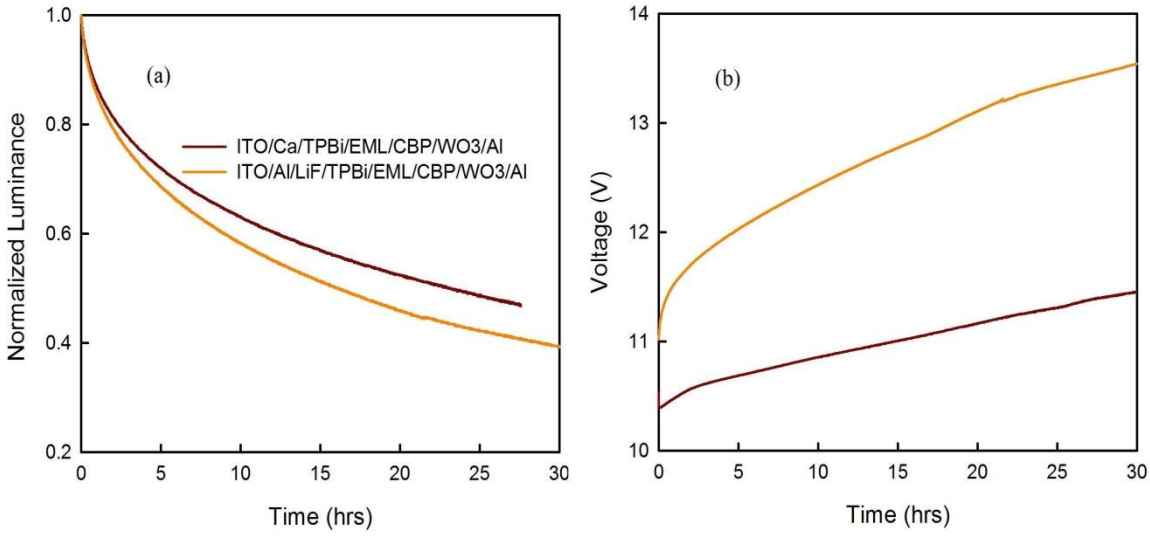

Figure 4.7 (a) Evolution of (a) normalized luminance over time and (b) voltage over time of inverted HyLEDs

4.4 Conclusions

We have successfully demonstrated green phosphorescent inverted bottom emission HyLEDs with an ITO bottom cathode and an Al top anode. Addition of nanometer-thick Ca, Al/LiF and Ca/LiF dramatically improved the device performance, by enhancing the electron injection from bottom ITO cathode into the organic layer. The device with a Ca injection layer showed the maximum luminance of 2780 Cd/m^2 and a turn-on voltage as low as 7 V. The device was also found to be stable under constant-current stressing. Therefore, the inverted bottom emitting HyLEDs fabricated in this work has a potential to be integrated with a-Si TFT for application in large active matrix OLED displays.

References

[1] T.Y. CHU et al. Jpn. J. Appl. Phys., Vol. 45, No. 6A (2006)

[2] Chen et al. Appl. Phys. Lett. 89, 053518, (2006).

[3] V. Bulovi, P. Tian, P.E. Burrows, M.R. Gokhale, S.R. Forrest, Appl. Phys. Lett. 70 (1997) 2954.

[4] X. Zhou, M. Pfeiffer, J.S. Huang, J. Blochwitz-Nimoth, D.S. Qin, A. Werner, J. Drechsel, B. Maennig, K. Leo, Appl. Phys. Lett. 81 (2002) 922.

[5] C. Qiu, H. Chen, Z. Xie, M. Wong, H.S. Kwok, Appl. Phys. Lett. 80 (2002) 3485.

[6] C.W. Chen, C.L. Lin, C.C. Wu, Appl. Phys. Lett. 85 (2004) 2469.

[7] Ho Won Choi, Soo Young Kim, Woong Kwon Kim, Jong Lam Lee, Appl. Phys. Lett. 87 (2005) 082102.

[8] Ta-Ya Chu, Jenn-Fang Chen, Szu-Yi Chen, Chao-Jung Chen, Chin H. Chen, Appl. Phys. Lett. 89 (2006) 053503.

[9] V. Bulovic, P. Tian, P. E. Burrows, M. R. Gokhale, S. R. Forrest and M. E. Thompson: Appl. Phys. Lett. 70 (1997) 2954.

[10] W. Kowalsky, E. Becker, T. Benstem, H.-H. Johannes, D. Metzdorf, H. Zeuner and J. Schobel: Proc. SPIE 4105 (2001) 194.

[11] T. Dobbertin, O. Werner, J. Meyer, A. Kammoun, D. Schneider, T. Riedl, E. Becker, H. H. Johannes and W. Kowalsky: Appl. Phys. Lett. 83 (2003) 5071.

[12] S. Kho, S. Sohn and D. Jung: Jpn. J. Appl. Phys. 42 (2003) L552.

[13] J. M. Zhao, Y. Q. Zhan, S. T. Zhang, X. J. Wang, Y. C. Zhou, Y. Wu, Z. J. Wang, X. M. Ding and X. Y. Hou: Appl. Phys. Lett. 84 (2004) 5377.

[14] S. Kho, S. Sohn and D. Jung: J. Korean Phys. Soc. 46 (2005) 1224.

[15] L. S. Liao, L. S. Hung, W. C. Chan, X. M. Ding, T. K. Sham, I. Bello, C. S. Lee and S. T. Lee: Appl. Phys. Lett. 75 (1999) 1619.

[16] T. Dobbertin, M. Kroeger, D. Heithecker, D. Schneider, D. Metzdorf, H. Neuner, E. Becker, H.-H. Johannes and W. Kowalsky: Appl. Phys. Lett. 82 (2003) 284.

[17] T. Dobbertin, O. Werner, J. Meyer, A. Kammoun, D. Schneider, T. Riedl, E. Becker, H.-H. Johannes and W. Kowalsky: Appl. Phys. Lett. 83 (2003) 5071.

[18] M. Pfeiffer, S. R. Forrest, X. Zhou and K. Leo: Org. Electron. 4 (2003) 21.

[19] H. W. Choi, S. Y. Kim, W.-K. Kim and J.-L. Lee: Appl. Phys. Lett. 87 (2005) 082102.

[20] L. Hou, F. Huang, W. Zeng, J. Peng and Y. Cao: Appl. Phys. Lett. 87 (2005) 153509.

[21] S.-W. Park, J.-M. Choi, E. Kim and S. Im: Appl. Surf. Sci. 244 (2005) 439.

[22] T. Miyashita, S. NaKa, H. Okada and H. Onnagawa: IDW '04 Dig., 2004, p. 1421.

[23] C.-W. Chen, C.-L. Lin and C.-C. Wu: Appl. Phys. Lett. 85 (2004) 2469.

[24] X. Zhu, J. Sun, H. Peng, M. Wong and H.-S. Kwok: SID Int. Symp. Dig. Tech. Pap. 35 (2005) 793.

[25] Y. Lee et al. Organic Electronics 9 (2008) 407–412

Chapter 5

Conclusions and Future Work

5.1 Conclusions

This thesis work focused on development of hybrid inorganic-organic light emitting diodes (HyLEDs) using metal oxides as charge transport layers. Firstly, zinc-tin-oxide (ZTO) thin films of various Zn and Sn compositions were prepared and their optical and electrical properties were studied.100 nm thin ZTO films of 0 to 1 at. % Sn (defined as Sn/Sn+Zn) were prepared by thermal co-evaporation using separate sources of ZnO and SnO_2. The as-deposited films were conductive but not transparent. Upon post-annealing in air, a sharp increase in transparency was observed between 350 - 550 ^oC, accompanying with a marked decrease in conductivity. This was attributed to re-oxidation of partially reduced oxides, leading to a lower density of oxygen vacancies. Also, thin films of tungsten oxide (WO_3) were prepared by thermal evaporation and their optical and electrical properties were studied. Results confirmed that the as-deposited films were highly transparent (90%) in the visible region and semiconducting (resistivity ~10^3 Ωcm). The study showed that conductive and transparent ZTO and WO_3 films may be prepared by thermal evaporation deposition, and are suitable for use in OLEDs as charge transport layers.

Secondly, we demonstrated high brightness green phosphorescent HyLED based on a simplified structure. 35 nm WO_3 was used as both the hole injection and transport layers. The WO_3 significantly improved the hole injection and transport, and thus balanced charge injection, leading to improved device efficiency and lifetime. Compared to all-organic LEDs, the current efficiency of the HyLED at 20 mA/cm2 was 57% higher and the half-life time under 20 mA/cm2

stressing was 7 times longer. This simplified hybrid structure represents a viable design for efficient and durable OLEDs suitable for display and lighting applications.

Finally, we fabricated inverted bottom emitting HyLEDs based on ITO as cathode and Al as anode. Addition of nanometer-thick Ca, Al/LiF and Ca/LiF dramatically improved the device performance, by enhancing the electron injection from bottom ITO cathode into the organic layer. The device with a Ca injection layer showed the maximum luminance of 2780 Cd/m^2 and a turn-on voltage as low as 7 V. The device was also found to be stable under constant-current stressing. Therefore, the inverted bottom emitting HyLEDs fabricated in this work has a potential to be integrated with a-Si TFT for application in large active matrix OLED displays.

5.2 Future Work

The performance of the developed HyLEDs and inverted structure HyLEDs may be further improved by replacing the organic ETL with an inorganic ETL. It has been proved that ZTO films prepared by thermal co-evaporation have good optical and electrical properties, but they are too rough. The release of oxygen and presence of micro-defects in the films are detrimental to the device performance and yield. An alternative deposition technique, like sputtering, may be used to prepare high-quality ZTO films. This should be applicable to the fabrication of inverted HyLEDs since the ZTO layer is deposited before the organic layers. Other potential inorganic electron transporting materials should be explored, including different TCOs and some oxygen-free semiconductors. They should be transparent to visible light and have a favorable conduction band aligned with the LUMO energy level of the organic EML.